Available online at www.sciencedirect.com
ScienceDirect
Journal of Computational Physics 221 (2007) 693–723
JOURNAL OF COMPUTATIONAL PHYSICS
www.elsevier.com/locate/jcp

Arbitrary high order non-oscillatory finite volume schemes on unstructured meshes for linear hyperbolic systems

Michael Dumbser [a,b,*], Martin Käser [b]

[a] *Institut für Aerodynamik und Gasdynamik, Pfaffenwaldring 21, D-70550 Stuttgart, Germany*
[b] *Laboratory of Applied Mathematics, University of Trento, Via Mesiano 77, 38050 Trento, Italy*

Received 12 January 2006; received in revised form 16 May 2006; accepted 26 June 2006
Available online 17 August 2006

Abstract

In this article we present a non-oscillatory finite volume scheme of arbitrary accuracy in space and time for solving linear hyperbolic systems on unstructured grids in two and three space dimensions using the ADER approach. The key point is a new reconstruction operator that makes use of techniques developed originally in the discontinuous Galerkin finite element framework. First, we use a hierarchical orthogonal basis to perform reconstruction. Second, reconstruction is not done in physical coordinates, but in a reference coordinate system which eliminates scaling effects and thus avoids ill-conditioned reconstruction matrices. In order to achieve non-oscillatory properties, we propose a new WENO reconstruction technique that does not reconstruct point-values but entire polynomials which can easily be evaluated and differentiated at any point. We show that due to the special reconstruction the WENO oscillation indicator can be computed in a mesh-independent manner by a simple quadratic functional. Our WENO scheme does not suffer from the problem of negative weights as previously described in the literature, since the linear weights are not used to increase accuracy. Accuracy is obtained by merely putting a large linear weight on the central stencil. The resulting one-step ADER finite volume scheme obtained in this way performs only one nonlinear WENO reconstruction per element and time step and thus can be implemented very efficiently even for unstructured grids in three space dimensions. We show convergence results obtained with the proposed method up to sixth order in space and time on unstructured triangular and tetrahedral grids in two and three space dimensions, respectively.

PACS: 02.70.Fj; 47.11.+j

MSC: 65M12; 76M25

Keywords: WENO reconstruction; ADER approach; Finite volume schemes; Unstructured meshes in two and three space dimensions; Linear hyperbolic systems

* Corresponding author. Address: Institut für Aerodynamik und Gasdynamik, Pfaffenwaldring 21, D-70550 Stuttgart, Germany. Tel.: +49 170 9360238; fax: +49 711 685 3438.
E-mail addresses: michael.dumbser@iag.uni-stuttgart.de (M. Dumbser), martin.kaeser@ing.unitn.it (M. Käser).

0021-9991/$ - see front matter © 2006 Elsevier Inc. All rights reserved.
doi:10.1016/j.jcp.2006.06.043

1. Introduction

The goal of our presented work is to construct a numerical method that can solve hyperbolic PDEs with, at least theoretically, arbitrary high order of accuracy in space and time in complex two and three-dimensional domains. Hence, the method should be able to run on unstructured meshes. Therefore, high order finite difference (FD) schemes are not an option due to their requirement of structured grids. Furthermore, the scheme should be able to treat discontinuous solutions without producing spurious oscillations. Finite volume (FV) methods have the advantage over finite difference schemes that they can be extended to high order of accuracy even on unstructured grids using a reconstruction operator. Previous work documented in the literature contains the use of linear reconstruction operators such as least-squares reconstruction [4,30], based on a single stencil. These linear operators, however, generate spurious oscillations in the vicinity of discontinuities. Therefore, nonlinear ENO reconstructions on unstructured grids have been introduced [1,37], as well as WENO reconstructions [23,36,17,27]. However, all the previously cited reconstruction operators have only been used in two space dimensions and the maximum achieved order documented in those publications was four. To our knowledge, no results of three-dimensional ENO or WENO schemes on unstructured tetrahedral grids have been published up to now.

In this article we first present a new linear polynomial reconstruction operator that uses hierarchical orthogonal basis functions in a reference coordinate system to rule out scaling effects and to obtain a very general formulation that facilitates implementation in two and three dimensions and can automatically achieve any desired order of accuracy. The details are given in Section 2. To obtain a non-oscillatory scheme, a nonlinear WENO reconstruction operator is subsequently constructed, based on the linear reconstruction applied to a set of stencils which are then weighted in a nonlinear, solution-dependent way. Due to the use of the special basis functions, the construction and implementation of the resulting WENO scheme can be done very easily even in three space dimensions, see Section 2.3. Once the reconstruction is available, an arbitrary high order accurate finite volume scheme can be constructed using the ADER approach of Toro et al. In this article we focus our considerations on the nonlinear reconstruction operator and fundamental numerics and therefore restrict the applications to linear hyperbolic systems.

In the ADER approach, the numerical flux function is based on the solution of generalized Riemann problems, where the initial data on both sides of the element interfaces are no longer piecewise constant as in the original approach of Godunov [18], but where the initial data is piecewise polynomial, in general separated by a jump at the interface. First ideas of this concept can be traced back to Ben-Artzi and Falcovitz [5], who developed a second-order FV scheme based on the solution of generalized Riemann problems. The idea of arbitrary high order generalized Riemann solvers was first developed by Toro et al. in a finite volume framework for linear equations on Cartesian grids [42,35,34]. They called their approach *ADER*, as abbreviation for "*A*rbitrary high order schemes using *der*ivatives". The extension to nonlinear hyperbolic conservation laws with source terms has then been achieved by Titarev and Toro using a WENO reconstruction technique on Cartesian grids [40,44,41,45]. With the work of Käser and Iske [27] the ADER finite volume approach was for the first time applied on unstructured meshes. They considered nonlinear scalar hyperbolic conservation laws and achieved fourth order of accuracy in space and time using a WENO reconstruction.

The fundamental ideas behind the generalized Riemann problem solvers are a temporal Taylor series expansion of the state at the interface, where then time derivatives are replaced by space derivatives using repeatedly the governing conservation law in differential form, which is the so-called Cauchy–Kovalewski or Lax–Wendroff procedure. However, the problem is that in general neither the state nor the derivatives are defined on the element interfaces where jumps are admitted. The idea is now to solve conventional homogeneous Riemann problems for the state and all space derivatives. This strategy defines the values of the state and the space derivatives on the element interfaces which can then be plugged into the Cauchy–Kovalewski procedure. In the linear case, special simplifications can be applied to increase efficiency. The construction of the scheme, called ADER-FV scheme in this article, is presented in detail in Section 3. It has uniform accuracy in space and time and is stable up to a Courant number of one in one space dimension [16]. Numerical convergence studies are performed up to seventh order of accuracy in space and time on an irregular triangular grid in two dimensions and up to sixth order on a regular tetrahedral grid in three dimensions, see Section 4. The non-oscillatory properties are finally studied on irregular unstructured two and three-dimensional grids in Section 5.

2. A new reconstruction technique

2.1. Reconstruction basis functions and transformation to the reference coordinate system

The main ingredient of the proposed arbitrary high order finite volume scheme is a new reconstruction algorithm that makes use of techniques developed originally in the discontinuous Galerkin (DG) framework. The computational domain Ω is discretized by conforming elements $T^{(m)}$, indexed by a unique mono-index m ranging from 1 to the total number of elements E. The elements are chosen to be triangles in 2D and tetrahedrons in 3D. The union of all elements is called the triangulation or tetrahedrization of the domain, respectively,

$$\mathscr{T}_\Omega = \bigcup_{m=1}^{E} T^{(m)}. \tag{1}$$

As usual for finite volume schemes, data is represented by the cell averages of a conserved quantity u inside an element $T^{(m)}$,

$$\bar{u}^{(m)} = \frac{1}{|T^{(m)}|} \int_{T^{(m)}} u \, \mathrm{d}V, \tag{2}$$

where $|T^{(m)}|$ denotes the volume of the element. In order to achieve high order of accuracy for the spatial discretization, we need to reconstruct higher order polynomials w from the given cell averages. We write the reconstruction polynomial for element $T^{(m)}$ as

$$w^{(m)}(\xi,\eta,\zeta) = \hat{w}_l^{(m)} \Psi_l(\xi,\eta,\zeta), \tag{3}$$

where ξ, η and ζ are the coordinates in a reference coordinate system, see Fig. 1, where also the reference elements T_E are defined. Throughout the whole paper we use classical tensor notation, which implies summation over each index appearing twice. Whereas the reconstructed degrees of freedom $\hat{w}_l^{(m)}$ are not space-dependent, the reconstruction basis functions Ψ_l are polynomials of degree M and depend on space. The index l ranges from *0* to its maximum value $L-1$, where $L = \frac{1}{2}(M+1)(M+2)$ and $L = \frac{1}{6}(M+1)(M+2)(M+3)$ are the numbers of reconstructed degrees of freedom in 2D and 3D, respectively, depending on the order of the reconstruction. We use the hierarchical orthogonal reconstruction basis functions that are given e.g. in [8,10] for triangles in 2D and tetrahedrons in 3D. The transformation from the physical coordinate system x–y–z into the reference coordinate system ξ–η–ζ is in three space dimensions defined by

$$\begin{aligned} x &= X_1^{(m)} + (X_2^{(m)} - X_1^{(m)})\xi + (X_3^{(m)} - X_1^{(m)})\eta + (X_4^{(m)} - X_1^{(m)})\zeta, \\ y &= Y_1^{(m)} + (Y_2^{(m)} - Y_1^{(m)})\xi + (Y_3^{(m)} - Y_1^{(m)})\eta + (Y_4^{(m)} - Y_1^{(m)})\zeta, \\ z &= Z_1^{(m)} + (Z_2^{(m)} - Z_1^{(m)})\xi + (Z_3^{(m)} - Z_1^{(m)})\eta + (Z_4^{(m)} - Z_1^{(m)})\zeta, \end{aligned} \tag{4}$$

where $X_i^{(m)}$, $Y_i^{(m)}$ and $Z_i^{(m)}$ denote the physical vertex coordinates of the considered element $T^{(m)}$. In two space dimensions, the same transformation applies for x and y, setting $\zeta = 0$. As short notation for the mapping and its inverse mapping from $\vec{\xi} = (\xi,\eta,\zeta)$ to $\vec{x} = (x,y,z)$ and vice versa with respect to the element $T^{(m)}$, we simply write

$$\vec{x} = \vec{x}(T^{(m)}, \vec{\xi}), \quad \vec{\xi} = \vec{\xi}(T^{(m)}, \vec{x}). \tag{5}$$

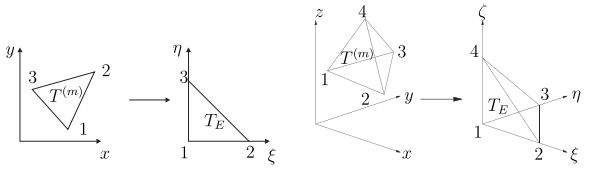

Fig. 1. Transformation from the physical triangle and tetrahedron $T^{(m)}$ to the canonical reference triangle T_E with nodes $(0,0)$, $(1,0)$ and $(0,1)$ and the canonical reference tetrahedron T_E with nodes $(0,0,0)$, $(1,0,0)$, $(0,1,0)$, $(0,0,1)$.

Via the inverse mapping given in (5) for the vector $\vec{\xi}$, the element $T^{(m)}$ is transformed to the unit element T_E, whose volume is $|T_E| = \frac{1}{2}$ in two dimensions and $|T_E| = \frac{1}{6}$ in three space dimensions, respectively. Furthermore,

$$J_{ij} = \frac{\partial x_i}{\partial \xi_j} \tag{6}$$

is the Jacobian matrix of the transformation and $|J| = |J_{ij}|$ its determinant, being equal to twice the triangle surface in 2D and equal to six times the tetrahedron volume in 3D.

For performing the reconstruction on element $T^{(m)}$, we now choose a reconstruction stencil

$$\mathscr{S}^{(m)} = \bigcup_{k=1}^{n_e} T^{(j(k))} \tag{7}$$

that contains a total number of n_e elements. Here $1 \leqslant k \leqslant n_e$ is a local index, counting the elements in the stencil, and $j = j(k)$ is the mapping from the local index k to the global indexation of the elements in $\mathscr{T}_\Omega$. We set by definition $j(1) = m$ and thus the first element in the stencil ($k = 1$) is always the considered element $T^{(m)}$ for which reconstruction is to be done. For ease of notation, we write in the following only j, meaning $j = j(k)$.

We then apply the inverse mapping (5) with respect to element $T^{(m)}$ to all the elements $T^{(j)} \in \mathscr{S}^{(m)}$, where the transformed elements are in the following denoted as $\tilde{T}^{(j)}$. We emphasize that for all elements $T^{(j)} \in \mathscr{S}^{(m)}$ the mapping with respect to the first element in the stencil is applied, so m is constant for each stencil and therefore the applied mapping formula is the *same* for all elements in $\mathscr{S}^{(m)}$. We note in particular that the transformed element of the first element in the stencil is of course the canonical reference element, hence $\widetilde{T}^{j(1)} = \widetilde{T}^{(m)} = T_E$. The stencil transformed in that way is denoted $\tilde{\mathscr{S}}^{(m)} = \bigcup \widetilde{T}^{(j)}$, see a two- and three-dimensional example in Figs. 2 and 3.

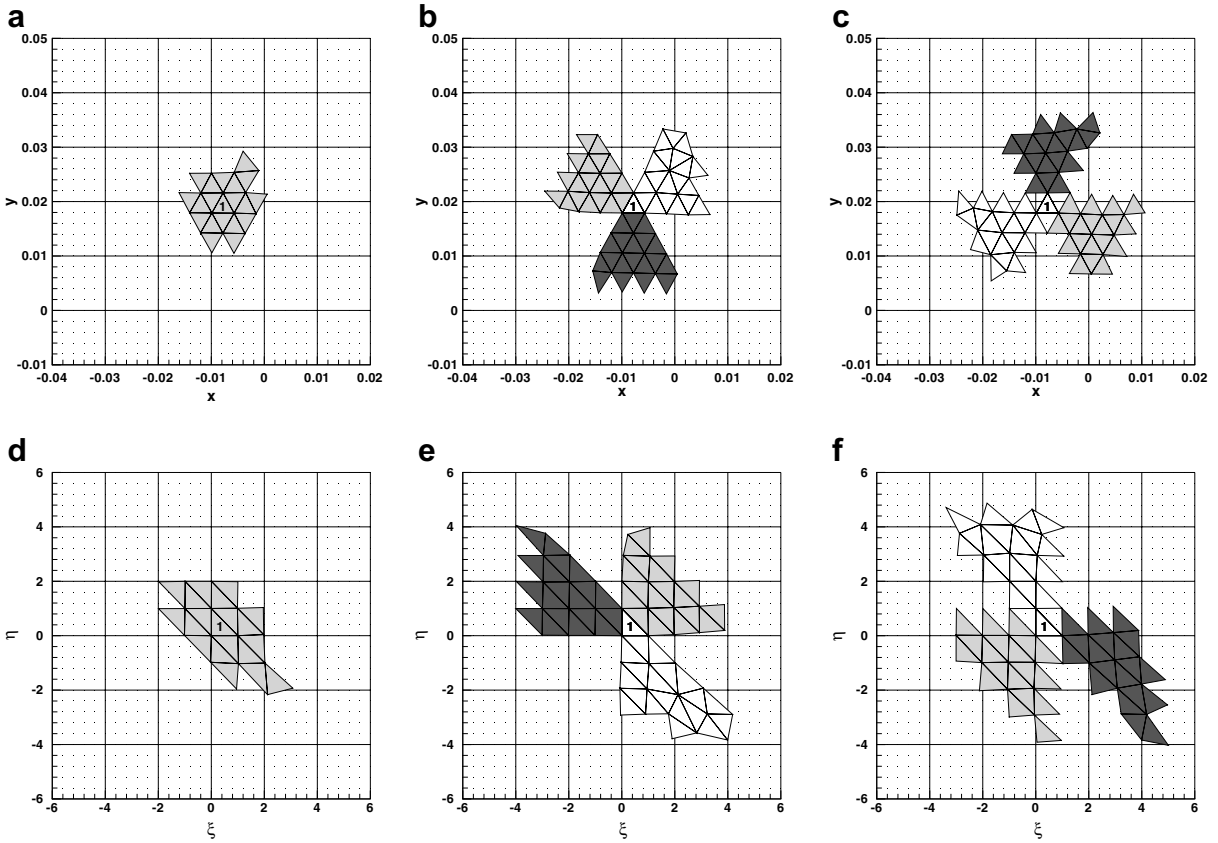

Fig. 2. Examples of original stencils $\mathscr{S}^{(m)}$ (top row) and transformed stencils $\tilde{\mathscr{S}}^{(m)}$ (bottom row) in 2D for third order polynomial reconstruction with $n_e = 20$. (a), (d): central WENO stencils. (b), (e): three primary WENO sector stencils. (c), (f): three reverse WENO sector stencils.

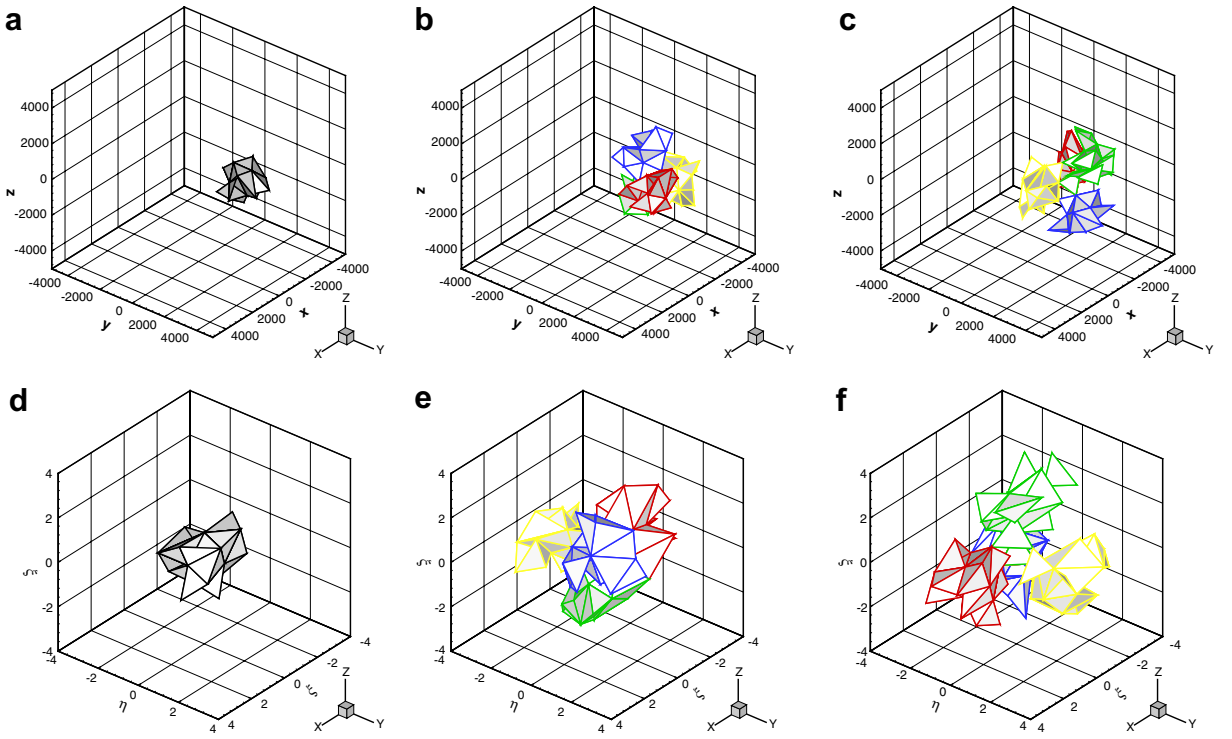

Fig. 3. Examples of original stencils $\mathscr{S}^{(m)}$ (top row) and transformed stencils $\tilde{\mathscr{S}}^{(m)}$ (bottom row) in 3D for second-order polynomial reconstruction with $n_e = 20$. (a), (d): central WENO stencils. (b), (e): four primary WENO sector stencils. (c), (f): four reverse WENO sector stencils.

The reconstruction must be conservative, at least in the element considered for reconstruction. Initially, we even require integral conservation for $w^{(m)}$ in all elements $T^{(j)} \in \mathscr{S}^{(m)}$. In the physical coordinate system we thus have

$$\int_{T^{(j)}} w^{(m)}(\vec{\xi}(T^{(m)},\vec{x}))\,\mathrm{d}V = |T^{(j)}|\bar{u}^{(j)}, \quad \forall T^{(j)} \in \mathscr{S}^{(m)}. \tag{8}$$

After transforming all elements of the stencil using (5) and taking into account that the degrees of freedom $\hat{w}_l^{(m)}$ do not depend on space, we obtain the intermediate result

$$|J|\left(\int_{\tilde{T}^{(j)}} \Psi_l(\vec{\xi})\,\mathrm{d}\xi\,\mathrm{d}\eta\,\mathrm{d}\zeta\right)\hat{w}_l^{(m)} = |J||\widetilde{T}^{(j)}|\bar{u}^{(j)}, \quad \forall \widetilde{T}^{(j)} \in \tilde{\mathscr{S}}^{(m)}. \tag{9}$$

The Jacobian determinant appears on both sides of Eq. (9) and thus cancels out. Please note that in the general case this is only possible for triangles and tetrahedrons with straight edges, to which we restrict ourselves in this paper. General polyhedral elements or even curved boundaries are not considered here.

The canceling of the Jacobian determinants automatically cancels scaling effects of the problem and avoids ill-conditioned reconstruction matrices as reported by Abgrall in [1]. Friedrich [17] used barycentric coordinates in order to avoid this problem, whereas we use a hierarchical *orthogonal* basis as commonly used in the discontinuous Galerkin finite element framework. During the reconstruction step, the basis polynomials are continuously extended over the whole stencil. In more detail, this extension means that during reconstruction the polynomial term given by $\Psi_l(\vec{\xi})$ is not only valid inside the reference element T_E, but also in all the other elements in the transformed stencil $\tilde{\mathscr{S}}^{(m)}$. After the reconstructed polynomial for element $T^{(m)}$ has been obtained, the basis polynomials are again restricted to the considered element $T^{(m)}$. We emphasize that the integration on the left hand side has to be done over the *transformed* elements $\widetilde{T}^{(j)}$. In order to do this integration, the trick now consists in doing *another* coordinate transformation to a second reference coordinate

system using the vertices of the transformed element $\widetilde{T}^{(j)}$ as parameter of another mapping from the first ξ–η–ζ reference system to the second $\tilde{\xi}-\tilde{\eta}-\tilde{\zeta}$ reference coordinate system. For convenience, we denote $\vec{\Xi}=(\tilde{\xi},\tilde{\eta},\tilde{\zeta})$. The mapping and its inverse are then denoted as

$$\vec{\xi}=\vec{\xi}(\widetilde{T}^{(j)},\vec{\Xi}),\quad \vec{\Xi}=\vec{\Xi}(\widetilde{T}^{(j)},\vec{\xi}), \tag{10}$$

and the Jacobian determinant of this mapping is called $|\tilde{J}|$. Thus, Eq. (9) becomes after the second transformation

$$|J||\tilde{J}|\left(\int_{T_E}\Psi_l(\vec{\xi}(\widetilde{T}^{(j)},\vec{\Xi}))\,\mathrm{d}\tilde{\xi}\,\mathrm{d}\tilde{\eta}\,\mathrm{d}\tilde{\zeta}\right)\hat{w}_l^{(m)}=|J||\tilde{J}||T_E|\bar{u}^{(j)},\quad \forall\widetilde{T}^{(j)}\in\tilde{\mathscr{S}}^{(m)}, \tag{11}$$

where again all Jacobian determinants cancel out! The final set of reconstruction equations is

$$\left(\int_{T_E}\Psi_l(\vec{\xi}(\widetilde{T}^{(j)},\vec{\Xi}))\,\mathrm{d}\tilde{\xi}\,\mathrm{d}\tilde{\eta}\,\mathrm{d}\tilde{\zeta}\right)\hat{w}_l^{(m)}=|T_E|\bar{u}^{(j)},\quad \forall\widetilde{T}^{(j)}\in\tilde{\mathscr{S}}^{(m)}. \tag{12}$$

In order to compute the integral on the left hand side of (12), we use classical multidimensional Gaussian quadrature of appropriate order. For an exhaustive overview of such multidimensional quadrature formulae see [38].

2.2. Solution of the reconstruction equations

The definition of the reconstruction equations (12) has been given in the previous section and for convenience, we introduce the simplified tensor notation

$$A_{kl}\hat{w}_l=\bar{u}_k, \tag{13}$$

with

$$A_{kl}=\frac{1}{|T_E|}\left(\int_{T_E}\Psi_l(\vec{\xi}(\widetilde{T}^{(j(k))},\vec{\Xi}))\,\mathrm{d}\tilde{\xi}\,\mathrm{d}\tilde{\eta}\,\mathrm{d}\tilde{\zeta}\right)\quad\text{and}\quad \bar{u}_k=\bar{u}^{(j(k))}. \tag{14}$$

The number of reconstructed degrees of freedom is L and therefore we need at least $n_e=L$ elements in the stencil. Unfortunately, if we choose $n_e=L$ so that the matrix A_{kl} becomes square, the resulting scheme may become unstable on general meshes. Therefore, we are forced to use *more* elements than the necessary minimum. The use of enlarged reconstruction stencils for robustness purposes has already been reported previously in the literature, see e.g. [4,30,27].

Furthermore, due to geometrical issues, the reconstruction matrix may be not invertible. This may happen for example when all elements are aligned on a straight line. Therefore, the stencil construction algorithm should avoid such cases. In our particular implementation, we compute the singular values of the matrix A_{kl} and check if some of them are zero. If so, we continue adding elements until none of the singular values is zero.

In order to fix parameters once and for all, since we are interested in a very general algorithm, we usually choose $n_e=1.5L$ in 2D and $n_e=2L$ in 3D. This means that we take between 50% and 100% more elements than the minimum necessary for reconstruction. This large number of elements may seem to be exaggerated in some cases. However, we will see later in our numerical experiments that our reconstruction is first nevertheless computationally quite cheap and second also very robust. Therefore we can admit this generous choice for the stencil size. We note in particular that with this choice, we did not encounter any singular reconstruction matrix in all computations presented in this article.

Since (13) becomes overdetermined with our choice $n_e>L$ we use a constrained least-squares technique in order to solve (13) respecting conservation in the first element $T^{(m)}$ of the stencil. Due to the special choice of the reconstruction basis functions, the equality constraint becomes simply $\hat{w}_0=\bar{u}^{j(1)}=\bar{u}^{(m)}$, which is written in tensor notation

$$C_l\hat{w}_l=R_i\bar{u}_i. \tag{15}$$

The vectors C_l and R_i contain only zeros except of the entries $C_0 = 1$ and $R_1 = 1$. The least-squares solution of (13) with the constraint (15) is obtained by seeking the minimum of the functional

$$f = (A_{kl}\hat{w}_l - \bar{u}_k) \cdot (A_{kj}\hat{w}_j - \bar{u}_k) - \lambda \cdot (C_l\hat{w}_l - R_i\bar{u}_i) \tag{16}$$

with respect to $\hat{w}_l$ and the Lagrange multiplicator λ used for coupling the constraint. Differentiation yields

$$\frac{\partial f}{\partial \hat{w}_l} = 2A_{kl}A_{kj}\hat{w}_j - 2A_{kl}\bar{u}_k - \lambda C_l = 0, \qquad \frac{\partial f}{\partial \lambda} = C_l\hat{w}_l - R_i\bar{u}_i = 0. \tag{17}$$

and the final equation system to solve for the vector of unknown reconstructed degrees of freedom $\hat{w}_l$ and the Lagrange multiplier λ becomes

$$\begin{pmatrix} 2A_{kl}A_{kj} & -C_l \\ C_l\delta_{lj} & 0 \end{pmatrix} \cdot \begin{pmatrix} \hat{w}_j \\ \lambda \end{pmatrix} = \begin{pmatrix} 2A_{kl}\bar{u}_k \\ R_i\bar{u}_i \end{pmatrix}. \tag{18}$$

Here, δ_{lj} is the Kronecker symbol. The matrix on the left hand side of (18) will be called reconstruction matrix in the following and in order to increase the speed of the algorithm, it is inverted and stored for each element of $\mathscr{T}_\Omega$ so that the unknown vector of the reconstructed degrees of freedom $\hat{w}_l$ can be easily calculated by a simple matrix–vector multiplication of the inverse reconstruction matrix and the vector of known cell averages $\bar{u}_k$ of the stencil $\mathscr{S}^{(m)}$. We note that most of the memory requirements of our proposed scheme are due to the storage of the inverse reconstruction matrix.

2.3. A new unstructured WENO scheme of arbitrary accuracy with non-negative weights

There has been a long quest documented in the research literature to circumvent Godunov's theorem, which states that any linear scheme of order higher than one is oscillatory. The basic idea to get high order and at the same time non-oscillatory properties is to introduce a nonlinearity in the scheme, where the reconstruction depends on the numerical solution itself. Reconstructions producing "smoother" solutions are preferred by the nonlinearity. The most frequently used schemes are TVD schemes for second order of accuracy, see e.g. [46,47,19,39,29], and weighted essentially non-oscillatory (WENO) schemes for accuracy higher than two. WENO schemes [25,23,3,17,27] are usually preferred with respect to the original essentially non-oscillatory (ENO) schemes [20,7] since they are more accurate, more robust, and can be implemented more efficiently. However, there are two considerable drawbacks, which probably prevented their implementation and application on three-dimensional unstructured meshes. On the one hand side they may become computationally quite expensive on unstructured meshes in 3D, and on the other hand side there may arise the problem of negative weights [36,23], depending on the grid geometry.

On unstructured 3D meshes, the optimal WENO schemes may get computationally very expensive because they reconstruct *point-values* in each Gaussian quadrature point that is needed in the finite volume context to evaluate the inter-cell fluxes and to compute source terms, if present. For each Gaussian point, the whole nonlinear reconstruction must be done again, and when Runge–Kutta time-integration is performed, it has to be done in all the Runge–Kutta substages. The classical WENO technique reconstructing point-values using an appropriately weighted nonlinear combination of lower order polynomials may be very efficient in one space dimension and generally on structured grids, where reconstruction can still be split into a set of purely one-dimensional sub-problems, but on unstructured multidimensional meshes the computational effort grows tremendously, especially if volume integrals of source terms have to be evaluated. Therefore, we propose a modified WENO scheme that in general follows closely the previous work done on WENO methods by Jiang and Shu [25], Shi, Hu and Shu [36,23] and Balsara and Shu [3], except of the fact that we do *not* reconstruct *point-values*, but *entire polynomials*. As we will see later, this approach simultaneously removes the problem of negative weights and reduces considerably the computational effort, especially because of our special reconstruction technique presented in the previous sections. A similar concept has already been used by Friedrich [17] and Käser and Iske [27], however their implementation was restricted to two space dimensions and did not go beyond fourth order of accuracy in space and time. Furthermore, they weighted all stencils equally. In contrast to this choice, we weight the central stencil with a large linear weight compared to the one-sided stencils since in smooth regions the central stencil usually provides the most stable reconstruction together with the highest quality.

Following the previous work on WENO schemes, instead of choosing only one stencil for reconstruction, we now have to do reconstruction on a whole family of stencils $\mathscr{S}_i^{(m)}$, where $1 \leqslant i \leqslant n_s$ is the local number of the stencil and n_s is the total number of stencils used for the WENO reconstruction. The set of reconstruction stencils used in order to perform reconstruction for element $T^{(m)}$ is chosen as follows:

- One central stencil, which is obtained by recursively adding successively the Neumann neighbors (i.e. the direct side neighbors) of the element $T^{(m)}$ and all Neumann neighbors of the elements added to the stencil so far, until the desired number of stencil elements n_e is reached. For an example of central stencils see Fig. 2(a) and (d) in two dimensions and Fig. 3(a) and (d) in three dimensions.
- Three primary sector stencils in 2D, see Fig. 2(b) and (e), and four primary sector stencils in 3D, see Fig. 3(b) and (e). The sectorial search is very easily implemented in the ξ–η–ζ reference coordinate system. Each primary sector is spanned by one vertex of the reference element T_E and the vectors connecting the vertex with the face opposite to this vertex. Transformed elements $\widetilde{T}^{(j)}$ within such a sector are then added successively as for the central stencil.
- For special locations of the discontinuities, the primary sector stencils may not be sufficient to find smooth stencils. Therefore, Käser and Iske [27] proposed to use also so-called reverse sectors, in order to have a greater choice of one-sided reconstructions. The center of each reverse sector is defined by one vertex of the reference element T_E plus the average of the vectors spanning the corresponding primary sector. The vectors spanning the reverse sector are simply the negative vectors spanning the corresponding primary sector. For examples, see Fig. 2(c) and (f) in 2D and Fig. 3(c) and (f) in 3D.

Therefore, we usually have a total set of $n_s = 7$ stencils in 2D and $n_s = 9$ stencils in 3D. n_s may be decreased in the presence of the boundary of Ω or if it is not possible to find full sets of primary and reverse sector stencils due to geometrical issues. We define the convention that the first stencil is always the central one. All stencils $\mathscr{S}_i^{(m)}$ are first transformed to the ξ–η–ζ reference system, then the reconstruction according to Eq. (12) is done for each of the transformed stencils $\tilde{\mathscr{S}}_i^{(m)}$. For each stencil in the set of stencils we obtain a vector of reconstructed degrees of freedom $\hat{w}_l^i$ solving (18).

Please note that the implementation of periodic boundary conditions becomes particularly easy due to the transformation to the reference coordinate system. For an element $T^{(m)}$ whose stencils are spread across a periodic boundary, it is sufficient to enforce continuity of the transformed stencils $\tilde{\mathscr{S}}_i^{(m)}$ in the reference system by mere translation of the mapped elements.

The final nonlinear WENO reconstruction polynomial $w_{\mathrm{WENO}}^{(m)}$ of degree M is now defined by a nonlinear combination of the polynomials $w_i^{(m)}$ of degree M, reconstructed on n_s stencils:

$$w_{\mathrm{WENO}}^{(m)}(\xi,\eta,\zeta) = \sum_{i=1}^{n_s} \omega_i w_i^{(m)}(\xi,\eta,\zeta) = \left(\sum_{i=1}^{n_s} \omega_i \hat{w}_l^i \right) \Psi_l(\xi,\eta,\zeta). \tag{19}$$

According to [25,3,23,27] we define the normalized nonlinear weights ω_i as

$$\omega_i = \frac{\tilde{\omega}_i}{\sum_{r=1}^{n_s} \tilde{\omega}_r}, \tag{20}$$

where the non-normalized nonlinear weights $\tilde{\omega}_i$ are functions of the linear weights λ_i and the so-called oscillation indicators σ_i as follows:

$$\tilde{\omega}_i = \frac{\lambda_i}{(\epsilon + \sigma_i)^r}. \tag{21}$$

According to the literature [27], we typically choose $\epsilon = 10^{-5}$ and $r = 4$. Up to now, no changes concerning the nonlinear weights used in the usual point-wise WENO reconstruction have been introduced. However, our choice of the linear weights λ_i and the oscillation indicator will be different. First, the linear weights are simply defined by

$$\lambda_i = \begin{cases} \lambda_1 \text{ if } i = 1, \\ 1 \quad \text{else.} \end{cases} \tag{22}$$

Since for smooth solutions the central stencil is usually the best one, we put a large linear weight $\lambda_1 \gg 1$ on the central stencil, which was by definition the first stencil in the whole set of stencils. The one-sided reconstruction stencils get the lower weight one. We usually take $\lambda_1 = 10^3$. However, as shown previously in the literature on WENO schemes for the parameters ϵ and r, our sensitivity studies carried out in Section 5.1 show that the results are not very sensitive to the choice of λ_1 in the range from 10^2 to 10^5. Lower values yield better results on discontinuities, larger values are usually better for smooth solutions.

Due to our reconstruction in the reference coordinate system, the oscillation indicators σ_i of each stencil can be computed in a mesh-independent manner as a quadratic functional of the reconstructed degrees of freedom $\hat{w}_l^i$. Due to the reference system, scaling is already taken out of the problem, therefore we do not need to consider the element's volume in the formula for the oscillation indicator as usually documented in the literature, see [27,23]. We compute σ_i as

$$\sigma_i = \sum_{r=1}^{M} \sum_{\alpha=0}^{r} \sum_{\beta=0}^{r-\alpha} \int_{T_E} \left(\frac{\partial^r}{\partial \xi^\alpha \partial \eta^\beta \partial \zeta^\gamma} w_i^{(m)}(\xi,\eta,\zeta) \right)^2 \mathrm{d}\xi\,\mathrm{d}\eta\,\mathrm{d}\zeta, \tag{23}$$

with $\gamma = r - \alpha - \beta$. Due to the definition (3) of the reconstructed polynomials in terms of reconstruction basis functions Ψ_l, we obtain the simple quadratic functional

$$\sigma_i = \hat{w}_l^i \Sigma_{lm} \hat{w}_m^i, \tag{24}$$

with the universal oscillation indicator matrix Σ_{lm},

$$\Sigma_{lm} = \sum_{r=1}^{M} \sum_{\alpha=0}^{r} \sum_{\beta=0}^{r-\alpha} \int_{T_E} \frac{\partial^r}{\partial \xi^\alpha \partial \eta^\beta \partial \zeta^\gamma} \Psi_l(\xi,\eta,\zeta) \cdot \frac{\partial^r}{\partial \xi^\alpha \partial \eta^\beta \partial \zeta^\gamma} \Psi_m(\xi,\eta,\zeta)\,\mathrm{d}\xi\,\mathrm{d}\eta\,\mathrm{d}\zeta, \tag{25}$$

which does neither depend on the mesh, nor on the problem. It just depends on the reconstruction basis functions and can be easily precomputed once, e.g. using modern computer algebra systems, and then stored. Please note that in (24) tensor summation only has to be done for indices l and m, whereas i is the index for the corresponding stencil.

3. Efficient formulation of the unstructured ADER finite volume scheme in two and three dimensions for linear hyperbolic systems

In this section we apply the reconstruction operator described in detail in Section 2 to construct an arbitrarily accurate finite volume scheme on two- and three-dimensional unstructured meshes using the ADER approach of Toro et al. [42,40,41,35,34]. For simplicity reasons, we restrict the application to general linear hyperbolic systems

$$\frac{\partial u_p}{\partial t} + A_{pq} \frac{\partial u_q}{\partial x} + B_{pq} \frac{\partial u_q}{\partial y} + C_{pq} \frac{\partial u_q}{\partial z} = 0, \tag{26}$$

in two and three space dimensions, where the two-dimensional case is obtained by simply setting $\frac{\partial}{\partial z} = 0$ and $C_{pq} = 0$. Again, we use classical tensor notation, which implies summation over each index appearing twice. The indices p and q range from 1 to the number of equations Q of the system. The resulting scheme will be a significant generalization of the approach presented in [34] for Cartesian meshes.

3.1. Semi-discrete form of the scheme

The computational domain is divided in conforming elements (triangles or tetrahedrons) $T^{(m)}$ being addressed by a unique index (m). The numerical solution u_h of (26) is approximated inside each element $T^{(m)}$ by the cell average of the state vector $\bar{u}_p$. The approximation space is denoted by V_h, which for finite volume schemes is the space of piecewise constant functions. The reconstruction space is the space of piecewise polynomials up to degree M and is denoted W_h. The reconstructed numerical solution $w_h \in W_h$ is given elementwise by (3), either obtained by using a linear reconstruction based on the central stencil only, or by using the WENO reconstruction procedure described in Section 2.3. For systems, we apply the WENO procedure

component-wise in this article. We note that a reconstruction of degree M leads to a scheme with accuracy $M+1$. Eq. (26) is now integrated over an element $T^{(m)}$

$$\int_{T^{(m)}} \frac{\partial u_p}{\partial t}\,\mathrm{d}V + \int_{T^{(m)}} \left(A_{pq}\frac{\partial u_q}{\partial x} + B_{pq}\frac{\partial u_q}{\partial y} + C_{pq}\frac{\partial u_q}{\partial z} \right) \mathrm{d}V = 0. \tag{27}$$

Integration by parts yields

$$\int_{T^{(m)}} \frac{\partial u_p}{\partial t}\,\mathrm{d}V + \int_{\partial T^{(m)}} F_p^h(w_q^-, w_q^+)\vec{n}\,\mathrm{d}S = 0, \tag{28}$$

where a numerical flux $F_p^h(w_q^-, w_q^+)\vec{n}$ depending on the reconstructed numerical solutions $w_q^{\pm}$ on the right and the left of the interface has been introduced in the surface integral since w_q is usually discontinuous at the element boundaries. The flux can be written very easily in a coordinate system which is aligned with the outward pointing unit normal vector $\vec{n} = (n_x, n_y, n_z)^{\mathrm{T}}$ on the boundary. The Jacobian matrix in normal direction A_{pq}^N is defined as

$$A_{pq}^N = A_{pq}n_x + B_{pq}n_y + C_{pq}n_z, \tag{29}$$

with its right and left eigenvector matrices R_{pq}^N and $L_{pq}^N = (R_{pq}^N)^{-1}$, respectively. The diagonal eigenvalue matrix is $\Lambda_{rs}^N = \mathrm{diag}(\lambda_1, \lambda_2, \ldots, \lambda_P)$ and thus $A_{pq}^N = R_{pr}^N \cdot \Lambda_{rs}^N \cdot L_{sq}^N$. The matrix absolute value operator is defined as

$$|A_{pq}^N| = R_{pr}^N \cdot |\Lambda_{rs}^N| \cdot L_{sq}^N, \tag{30}$$

with $|\Lambda_{rs}^N| = \mathrm{diag}(|\lambda_1|, |\lambda_2|, \ldots, |\lambda_P|)$. We use the exact Riemann solver as numerical flux between two elements $T^{(m)}$ and $T^{(k_j)}$:

$$F_p^h(w_q^-, w_q^+)\vec{n} = \frac{1}{2}[(A_{pq}^{N_j} + |A_{pq}^{N_j}|)w_q^- + (A_{pq}^{N_j} - |A_{pq}^{N_j}|)w_q^+], \tag{31}$$

where $w_q^- = \hat{w}_{ql}^{(m)}\Psi_l^{(m)}$ and $w_q^+ = \hat{w}_{ql}^{(k_j)}\Psi_l^{(k_j)}$ are the boundary extrapolated values of the reconstructed numerical solution w_h from element (m) and the jth side neighbor (k_j), respectively, since both elements adjacent to a boundary contribute to the numerical flux. The superscript N_j indicates that for each face of the element the Jacobian matrix in normal direction has to be evaluated according to the corresponding normal vector of the face. For rotationally invariant systems, special simplifications can be applied, see [11]. For non-conservative linear systems with piecewise constant varying coefficients, the same flux formulation is valid, with the only modification that the flux has to be evaluated in each element with the corresponding coefficient matrix $A_{pq}^{N_j} = A_{pq}^{N_j}(T^{(m)})$ as function of the element $T^{(m)}$. Inserting (31) into (28) and splitting the boundary integral into the contributions of each face $1 \leqslant j \leqslant N_E$ of the element $T^{(m)}$, we obtain

$$\frac{\partial}{\partial t}\hat{u}_p^{(m)} \int_{T^{(m)}} \mathrm{d}V + \sum_{j=1}^{N_E} \frac{1}{2}(A_{pq}^{N_j} + |A_{pq}^{N_j}|)\hat{w}_{ql}^{(m)} \int_{(\partial T^{(m)})_j} \Psi_l^{(m)}\,\mathrm{d}S + \sum_{j=1}^{N_E} \frac{1}{2}(A_{pq}^{N_j} - |A_{pq}^{N_j}|)\hat{w}_{ql}^{(k_j)} \int_{(\partial T^{(m)})_j} \Psi_l^{(k_j)}\,\mathrm{d}S = 0. \tag{32}$$

Eq. (32) is written in the physical x–y–z system, but if we transform each physical element $T^{(m)}$ to a canonical reference element T_E in a ξ–η–ζ reference system (see Fig. 1), the method can be implemented much more efficiently since all integrals can be precomputed beforehand in the reference system.

After integration in the reference system, the semi-discrete formulation in 2D and 3D then reads as

$$\frac{\partial}{\partial t}\bar{u}_p^{(m)}|T^{(m)}| + \sum_{j=1}^{N_E} \frac{1}{2}(A_{pq}^{N_j} + |A_{pq}^{N_j}|)|S_j|F_l^{-,j}\hat{w}_{ql}^{(m)} + \sum_{j=1}^{N_E} \frac{1}{2}(A_{pq}^{N_j} - |A_{pq}^{N_j}|)|S_j|F_l^{+,i,h}\hat{w}_{ql}^{(k_j)} = 0, \tag{33}$$

where $|S_j|$ denotes the surface of face j in 3D and the edge length of edge j in 2D. In (33) we use flux matrices acting on the degrees of freedom of the reconstructed polynomials similar to the flux matrices for ADER-DG schemes introduced in [11,14,13], which act on the degrees of freedom of the DG basis polynomials. The flux matrices can be calculated analytically once on the reference element and then be stored. In the following, we give the details of calculating those flux matrices on triangles and tetrahedrons in two and three space dimensions. First, we define the local faces with their local vertex ordering according to Table 1, where the vertex

Table 1
Face definition on triangles and tetrahedrons

Triangles (2D)			Tetrahedrons (3D)			
Face	Points		Face	Points		
1	1	2	1	1	3	2
2	2	3	2	1	2	4
3	3	1	3	1	4	3
			4	2	3	4

numbering is strictly counter-clockwise in 2D as well as in 3D. Then, the vector of volume coordinates $\vec{\xi}$ is given on the faces via mapping functions from the face parameters χ and τ, see Tables 2 and 3. Last but not least, for flux computation over the face, we have to integrate along the face inside the element as well as in the neighbor. This is done consistently by the transformation from the face parameters χ and τ inside the element to the corresponding face parameters $\tilde{\chi}$ and $\tilde{\tau}$ in the neighbor face. Whereas in 2D this transformation is always $\tilde{\chi} = 1 - \chi$, in 3D the transformation depends on the orientation of the neighbor face respect to the local face of the considered element, since via rotation of the triangular faces there may be three possible orientations. The corresponding mappings are given in Table 4.

In two space dimensions, all possible flux matrices are

$$F_l^{-,j} = \int_{\partial(T_E)_j} \Psi_l(\vec{\xi}^{(j)}(\chi))\,\mathrm{d}\chi, \quad \forall 1 \leqslant j \leqslant 3, \tag{34}$$

$$F_l^{+,i,h} = \int_{\partial(T_E)_j} \Psi_l(\vec{\xi}^{(i)}(1-\chi))\,\mathrm{d}\chi, \quad \forall 1 \leqslant i \leqslant 3. \tag{35}$$

Index h is not used in 2D. In three dimensions, all possible flux matrices are

$$F_l^{-,j} = \int_{\partial(T_E)_j} \Psi_l(\vec{\xi}^{(j)}(\chi,\tau))\,\mathrm{d}\chi\,\mathrm{d}\tau, \quad \forall 1 \leqslant j \leqslant 4, \tag{36}$$

$$F_l^{+,i,h} = \int_{\partial(T_E)_j} \Psi_l(\vec{\xi}^{(i)}(\tilde{\chi}^{(h)},\tilde{\tau}^{(h)}))\,\mathrm{d}\chi\,\mathrm{d}\tau, \quad \forall 1 \leqslant i \leqslant 4,\ \forall 1 \leqslant h \leqslant 3. \tag{37}$$

Table 2
2D volume coordinates $\vec{\xi}^{(j)}$ in function of the edge parameter χ

j	1	2	3
$\xi^{(j)}(\chi)$	χ	$1-\chi$	0
$\eta^{(j)}(\chi)$	0	χ	$1-\chi$

Table 3
3D volume coordinates $\vec{\xi}^{(j)}$ in function of the face parameters χ and τ

j	1	2	3	4
$\xi^{(j)}(\chi,\tau)$	τ	χ	0	$1-\chi-\tau$
$\eta^{(j)}(\chi,\tau)$	χ	0	τ	χ
$\zeta^{(j)}(\chi,\tau)$	0	τ	χ	τ

Table 4
Transformation of the face parameters χ and τ of the tetrahedron's face to the face parameters $\tilde{\chi}$ and $\tilde{\tau}$ in the neighbor tetrahedron according to the three possible orientations (h) of the neighbor face

h	1	2	3
$\tilde{\chi}^{(h)}(\chi,\tau)$	τ	$1-\chi-\tau$	χ
$\tilde{\tau}^{(h)}(\chi,\tau)$	χ	τ	$1-\chi-\tau$

The left state flux matrix (superscript '−') $F_l^{-,j}$ accounts for the contribution of the element (m) itself to the fluxes over face j and the right state flux matrix (superscript '+') $F_l^{+,i,h}$ accounts for the contribution of the element's direct side neighbors (k_j) to the fluxes over the face j. Index $1 \leqslant i \leqslant N_E$ indicates the local number of the common face as it is seen from neighbor (k_j) and depends on the mesh generator. For tetrahedrons, index $1 \leqslant h \leqslant 3$ indicates the orientation of the nodes in the local face of neighbor (k_j) which lies on the local vertex 1 on the edge j in tetrahedron number (m) and depends also on the mesh generator. On a given tetrahedral mesh, where indices i and h are known, only four of the 12 possible matrices $F_l^{+,i,h}$ are used per element.

If we integrate the semi-discrete Eq. (33) in time with a Runge–Kutta method, we obtain a quadrature-free Runge–Kutta finite volume scheme. This would in fact be a similar approach for finite volume schemes as the one developed by Atkins and Shu in [2] for discontinuous Galerkin finite elements. However, in this article we do not use the Runge–Kutta method for time-integration, but we follow the ADER approach of Toro et al. as presented in the following section.

3.1.1. The fully discrete formulation of the ADER-FV scheme

Since the efficiency of Runge–Kutta time discretization schemes drastically decreases if the order of accuracy becomes greater than four, due to the so-called Butcher barriers [6], which cause the number of intermediate RK stages to become larger than the formal order of accuracy, we apply the ADER approach of Toro et al. to the semi-discrete form of the scheme (33) in order to achieve an arbitrarily accurate time discretization.

The main ingredients of the ADER approach are a Taylor expansion in time, the solution of generalized Riemann problems (GRP) to approximate the space derivatives at the interface and the Cauchy–Kovalewski procedure for replacing the time derivatives in the Taylor series by space derivatives. This is described in more detail in [11,15,44,41,45] for the nonlinear case. In this section we show how the ADER approach can be used for high order time-integration of the finite volume method on unstructured grids, called ADER-FV method in the following, for general linear hyperbolic systems. For linear systems, a particular simplification can be introduced: time-integration and flux computation can be exchanged, i.e. instead of solving the Riemann problems for all spatial derivatives on the interface and doing then the Cauchy–Kovalewski procedure with the obtained derivatives, we can integrate the reconstructed solution in time separately in each element using the Cauchy–Kovalewski procedure on the reconstructed solution and then plug the time-integrated values on the boundaries into the numerical flux function, which then takes correctly into account the discontinuity at the interface. We emphasize that the pure application of the Cauchy–Kovalewski procedure requires the solution to be analytic, whereas the ADER approach uses the solution of generalized Riemann problems with piecewise polynomial initial data. This supposes only that the solution is *piecewise* analytic on both side of the element interfaces. Note that the GRPs are always solved along the face-normal direction.

For the development of ADER-FV schemes, we first need a general formula for the Cauchy–Kovalewski procedure in order to replace the kth time derivative by pure space derivatives. Since all our basis functions are given in the ξ–η–ζ system, we need a Cauchy–Kovalewski procedure, which makes use of the spatial derivatives with respect to ξ, η and ζ. Therefore, we rewrite our original PDE (26) with the use of (6). With the definitions (38)–(40),

$$A^*_{pq} = A_{pq}\xi_x + B_{pq}\xi_y + C_{pq}\xi_z, \tag{38}$$

$$B^*_{pq} = A_{pq}\eta_x + B_{pq}\eta_y + C_{pq}\eta_z, \tag{39}$$

$$C^*_{pq} = A_{pq}\zeta_x + B_{pq}\zeta_y + C_{pq}\zeta_z, \tag{40}$$

we finally obtain

$$\frac{\partial u_p}{\partial t} + A^*_{pq}\frac{\partial u_q}{\partial \xi} + B^*_{pq}\frac{\partial u_q}{\partial \eta} + C^*_{pq}\frac{\partial u_q}{\partial \zeta} = 0. \tag{41}$$

The kth time derivative as a function of pure space derivatives in the ξ–η–ζ reference system is the result of the Cauchy–Kovalewski procedure applied to (41) and is given by

$$\frac{\partial^k u_p}{\partial t^k} = (-1)^k \left(A^*_{pq} \frac{\partial}{\partial \xi} + B^*_{pq} \frac{\partial}{\partial \eta} + C^*_{pq} \frac{\partial}{\partial \zeta} \right)^k u_q. \tag{42}$$

This can easily be proven by complete induction. It is a key point to use the Cauchy–Kovalewski procedure in the form (42) since it allows us to pre-calculate many matrices beforehand, as we will see in the following.

We expand the reconstructed solution of (26) in a Taylor series in time about the current time level t^n up to degree M,

$$w_p(\xi,\eta,\zeta,t) = \sum_{k=0}^{M} \frac{(t-t^n)^k}{k!} \frac{\partial^k}{\partial t^k} w_p(\xi,\eta,\zeta,t^n), \tag{43}$$

and replace time derivatives by space derivatives, using Eq. (42)

$$w_p(\xi,\eta,\zeta,t) = \sum_{k=0}^{M} \frac{(t-t^n)^k}{k!} (-1)^k \left(A^*_{pq} \frac{\partial}{\partial \xi} + B^*_{pq} \frac{\partial}{\partial \eta} + C^*_{pq} \frac{\partial}{\partial \zeta} \right)^k w_q(\xi,\eta,\zeta,t^n). \tag{44}$$

We now introduce the approximation (3) and obtain

$$w_p(\xi,\eta,\zeta,t) = \sum_{k=0}^{M} \frac{(t-t^n)^k}{k!} (-1)^k \left(A^*_{pq} \frac{\partial}{\partial \xi} + B^*_{pq} \frac{\partial}{\partial \eta} + C^*_{pq} \frac{\partial}{\partial \zeta} \right)^k \Psi_l\left(\vec{\xi}\right) \hat{w}_{ql}(t^n). \tag{45}$$

This approximation can now be projected onto the reconstruction basis functions Ψ_k in order to get an approximation of the evolution of the reconstructed degrees of freedom during one time step from time level t^n to time level t^{n+1}. We obtain

$$\hat{w}_{pl}(t) = \frac{\left\langle \Psi_n, \sum_{k=0}^{M} \frac{(t-t^n)^k}{k!} (-1)^k \left(A^*_{pq} \frac{\partial}{\partial \xi} + B^*_{pq} \frac{\partial}{\partial \eta} + C^*_{pq} \frac{\partial}{\partial \zeta} \right)^k \Psi_m \right\rangle}{\langle \Psi_n, \Psi_l \rangle} \hat{w}_{qm}(t^n), \tag{46}$$

where $\langle \cdot, \cdot \rangle$ denotes the inner product over the reference element T_E and the division by $\langle \Psi_n, \Psi_l \rangle$ denotes the multiplication with the inverse of the mass matrix. This reduces indeed to division by its diagonal entries since the mass matrix is diagonal due to the supposed orthogonality of the basis functions. Eq. (46) can be integrated analytically in time from the current time level t^n to the next time level $t^{n+1} = t^n + \Delta t$. We obtain

$$\int_{t^n}^{t^n+\Delta t} \hat{w}_{pl}(t)\,\mathrm{d}t = \frac{\left\langle \Psi_n, \sum_{k=0}^{M} \frac{\Delta t^{(k+1)}}{(k+1)!} (-1)^k \left(A^*_{pq} \frac{\partial}{\partial \xi} + B^*_{pq} \frac{\partial}{\partial \eta} + C^*_{pq} \frac{\partial}{\partial \zeta} \right)^k \Psi_m \right\rangle}{\langle \Psi_n, \Psi_l \rangle} \hat{w}_{qm}(t^n). \tag{47}$$

With the definition

$$I_{plqm}(\Delta t) = \frac{\left\langle \Psi_n, \sum_{k=0}^{M} \frac{\Delta t^{(k+1)}}{(k+1)!} (-1)^k \left(A^*_{pq} \frac{\partial}{\partial \xi} + B^*_{pq} \frac{\partial}{\partial \eta} + C^*_{pq} \frac{\partial}{\partial \zeta} \right)^k \Psi_m \right\rangle}{\langle \Psi_n, \Psi_l \rangle}. \tag{48}$$

Eq. (47) becomes simply

$$\int_{t^n}^{t^n+\Delta t} \hat{w}_{pl}(t)\,\mathrm{d}t = I_{plqm}(\Delta t) \hat{w}_{qm}(t^n). \tag{49}$$

For efficient algorithms to do the Cauchy–Kovalewski procedure, we refer to [11,26,12]. We finally obtain the fully discrete ADER-FV scheme by integration of (33) in time, where the superscripts n and $n+1$ denote the current and the successive time level

$$\begin{aligned} &[(\bar{u}_p^{(m)})^{n+1} - (\bar{u}_p^{(m)})^n] |T^{(m)}| + \frac{1}{2} \sum_{j=1}^{N_E} (A^{N_j}_{pq} + |A^{N_j}_{pq}|) |S_j| F^{-,j}_l \cdot I_{qlrm}(\Delta t) (\hat{w}^{(m)}_{rm})^n \\ &+ \frac{1}{2} \sum_{j=1}^{N_E} (A^{N_j}_{pq} - |A^{N_j}_{pq}|) |S_j| F^{+,i,h}_l \cdot I_{qlrm}(\Delta t) (\hat{w}^{(k_j)}_{rm})^n = 0. \end{aligned} \tag{50}$$

From the structure of Eq. (50) we see that the space–time-integrated values on the boundaries enter the exact Riemann solver in order to give the space–time integral of the solution of the GRP at the interface. We emphasize that this can only be done for linear systems.

The reconstructed degrees of freedom $(\hat{w}_{rm}^{(m)})^n$ at time level t^n are obtained for each element at the beginning of a time step using the reconstruction operator described in Section 2. On rectangular quadrilaterals and hexahedra, the scheme takes the same form. The proposed finite volume scheme is quadrature-free since no Gaussian integration is used in space and time. It performs high order time-integration from t^n to t^{n+1} in one single step. It thus needs the same memory as a first order explicit Euler time-stepping scheme. Please note that in order to perform convergence studies with analytical reference data using high order accurate finite volume schemes, the initial condition at t^0 must be projected onto the cell average via L^2 projection using high order Gaussian quadrature rules, otherwise at most second order can be achieved due to insufficient accuracy of the projection of the initial condition.

4. Numerical convergence results

In order to check the convergence of the proposed arbitrary high order finite volume scheme, we solve the linearized Euler equations in the 2D domain $\Omega_{2D} = [-50;50]\times[-50;50]$ with four periodic boundary conditions and in the 3D domain $\Omega_{3D} = [-50;50]\times[-50;50]\times[-50;50]$ with six periodic boundary conditions. The Jacobians of the linearized Euler equations are

$$A_{pq} = \begin{pmatrix} u_0 & \rho_0 & 0 & 0 & 0 \\ 0 & u_0 & 0 & 0 & \frac{1}{\rho_0} \\ 0 & 0 & u_0 & 0 & 0 \\ 0 & 0 & 0 & u_0 & 0 \\ 0 & \gamma p_0 & 0 & 0 & u_0 \end{pmatrix}, \quad B_{pq} = \begin{pmatrix} v_0 & 0 & \rho_0 & 0 & 0 \\ 0 & v_0 & 0 & 0 & 0 \\ 0 & 0 & v_0 & 0 & \frac{1}{\rho_0} \\ 0 & 0 & 0 & v_0 & 0 \\ 0 & 0 & \gamma p_0 & 0 & v_0 \end{pmatrix}, \quad C_{pq} = \begin{pmatrix} w_0 & 0 & 0 & \rho_0 & 0 \\ 0 & w_0 & 0 & 0 & 0 \\ 0 & 0 & w_0 & 0 & 0 \\ 0 & 0 & 0 & w_0 & \frac{1}{\rho_0} \\ 0 & 0 & 0 & \gamma p_0 & w_0 \end{pmatrix}. \tag{51}$$

The state vector contains the five fluctuation variables for density, velocity and pressure, i.e. $u_p = (\rho, u, v, w, p)^{\mathrm{T}}$. The initial condition is given as

$$u_p(x,y,z,0) = \begin{pmatrix} \sin(\vec{k}\vec{x}) & 0 & 0 & 0 & 0 \end{pmatrix}^{\mathrm{T}}, \tag{52}$$

with the wave-number vector $\vec{k} = \left(\frac{2\pi}{100}, \frac{2\pi}{100}, \frac{2\pi}{100}\right)^{\mathrm{T}}$ in three space dimensions. In two space dimensions, the last entry of $\vec{k}$ can be dropped. We set $\gamma = 1.4$, $\rho_0 = 1$, $u_0 = v_0 = w_0 = 1$ and $p_0 = \frac{1}{\gamma}$. After one advection period (time $t = 100$), the exact solution is given by the initial condition. We now perform two different types of convergence studies using either only linear reconstruction based merely on the central stencil or using the nonlinear WENO reconstruction. The meshes used are a sequence of very irregular triangular meshes in two dimensions, see Fig. 4 (top), obtained by successive red-refinement [28,21,22] and a sequence of regular tetrahedral grids, see Fig. 4 (bottom).

For measuring the error between the numerical solution of the first variable and the exact solution u_e of the first variable of the system, we first apply the reconstruction operator in order to get w_h from u_h and then we use the continuous L^p-norms

$$\|w_h - u_e\|_{L^p(\Omega)} = \left(\int_\Omega |w_h - u_e|^p \, \mathrm{d}V \right)^{\frac{1}{p}}, \tag{53}$$

in which the integration has been approximated using Gaussian integration formulae with twice the order of accuracy of the numerical scheme. The L_∞ norm has been approximated by taking the maximum error arising in any of the Gaussian integration points.

Tables 5–8 contain in the first row the mesh spacing h, which is taken as the maximum diameter of the outer circle and outer sphere of the triangles and the tetrahedrons, respectively. The next three rows contain the error measured in L^∞, L^1 and L^2 norm according to (53), followed by three columns giving the measured order of accuracy between the respective grid and the previous grid. The last row gives the CPU time needed by the

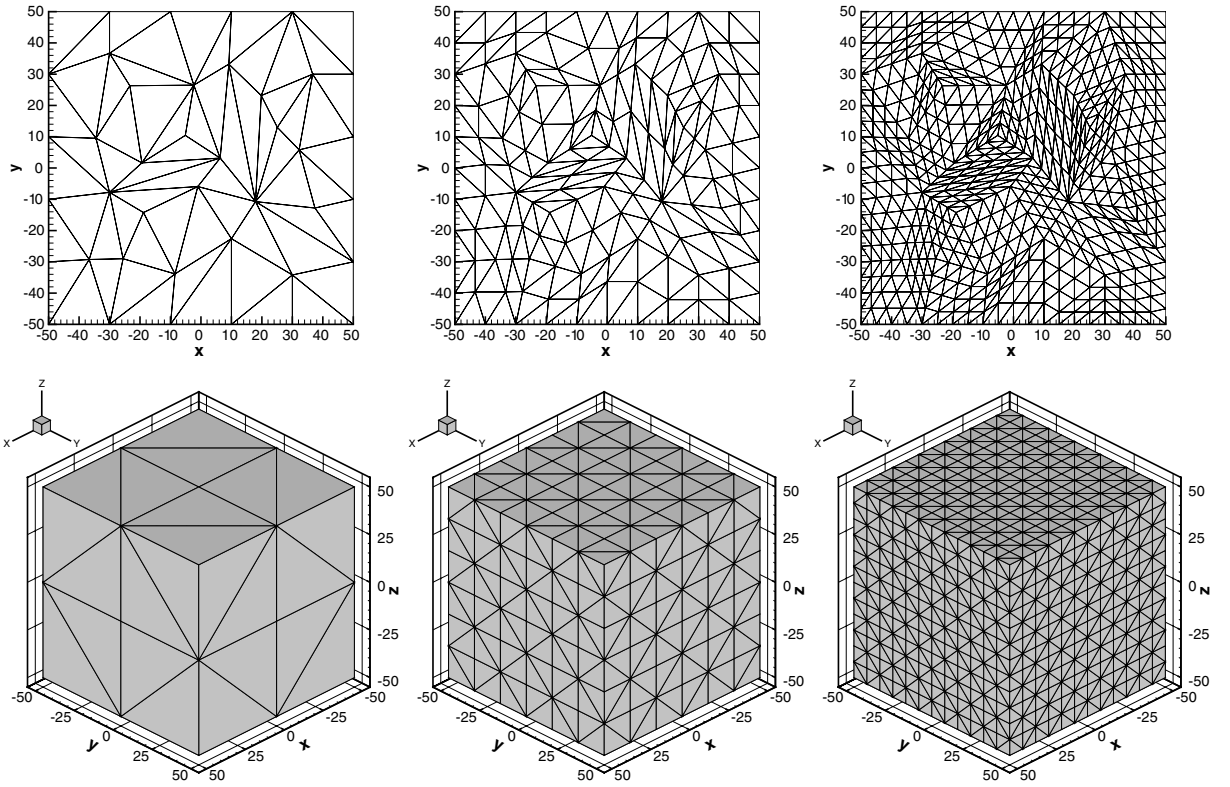

Fig. 4. Sequences of red-refined irregular meshes used for the two-dimensional convergence studies (top), and of regular grids used for the three-dimensional convergence studies (bottom).

serial code on a 2×3, 6 GHz Intel Dual Xeon workstation with 4 GB of RAM. A graphical illustration of the L^{∞} in terms of reciprocal mesh spacing $1/h$ and CPU time is given in Fig. 5. We see that in almost all cases the designed order of accuracy has been reached very well, for the linear schemes as well as for the nonlinear WENO schemes. Having a closer look at the CPU times, which were all measured on the same machine under the same conditions, we find a remarkable result: the nonlinear WENO reconstruction increases the total CPU time of the scheme at most by a factor of two compared to the linear reconstruction based on the central stencil, although for WENO we have to do reconstruction on 7 and 9 stencils in 2D and 3D, respectively. This is a strong indication that in general our reconstruction procedure is computationally quite efficient and that the overhead associated with the computation of the oscillation indicators and the nonlinear weights is quite small. Due to the quadrature-free high order accurate flux calculation in time via the ADER approach, our proposed finite volume scheme is a one-step scheme that does the WENO reconstruction only once per time step, which is a further benefit with respect to computational efficiency. Furthermore, we can deduce from Fig. 5 that activating the WENO procedure does not significantly decrease accuracy in comparison to the linear reconstruction based on the central stencil.

5. Numerical experiments showing the non-oscillatory properties

5.1. Sensitivity study with respect to the linear weight of the central stencil

WENO schemes have become very popular since they provide essentially non-oscillatory solutions, without having to adjust parameters. Of course, there are the parameters ϵ and r, and in our new formulation there even is an additional third parameter λ_1. However, WENO schemes can be considered almost parameter-free, since it has been shown in the research literature that the quality of the solution does not depend much on the

Table 5
Two-dimensional ADER finite volume schemes from second to seventh order in space and time using a linear reconstruction based only on the central stencil

h	L^∞	L^1	L^2	$\mathcal{O}_{L^\infty}$	$\mathcal{O}_{L^1}$	$\mathcal{O}_{L^2}$	t_{CPU} [s]
ADER-FV $\mathcal{O}2$, ($M=1$), 2D linear reconstruction							
4.23	1.1317E−01	3.4281E+02	4.0616E+00	0.0	0.0	0.0	4.95
2.11	2.9798E−02	7.4694E+01	8.7893E−01	1.9	2.2	2.2	36.48
1.06	6.6298E−03	1.7565E+01	2.0248E−01	2.2	2.1	2.1	279.64
0.53	1.7215E−03	4.3423E+00	4.9498E−02	1.9	2.0	2.0	2184.70
ADER-FV $\mathcal{O}3$, ($M=2$), 2D linear reconstruction							
4.23	5.1329E−02	2.2599E+02	2.5253E+00	0.0	0.0	0.0	6.69
2.11	8.0704E−03	3.2031E+01	3.5884E−01	2.7	2.8	2.8	50.75
1.06	1.0198E−03	4.2218E+00	4.7291E−02	3.0	2.9	2.9	394.70
0.53	1.2885E−04	5.4068E−01	6.0526E−03	3.0	3.0	3.0	3158.52
ADER-FV $\mathcal{O}4$, ($M=3$), 2D linear reconstruction							
4.23	6.3933E−03	1.0848E+01	1.3583E−01	0.0	0.0	0.0	10.91
2.11	4.7926E−04	6.1602E−01	7.9070E−03	3.7	4.1	4.1	83.67
1.06	3.8082E−05	3.4599E−02	4.4612E−04	3.7	4.2	4.1	658.02
0.53	2.5182E−06	2.1368E−03	2.7043E−05	3.9	4.0	4.0	5263.42
ADER-FV $\mathcal{O}5$, ($M=4$), 2D linear reconstruction							
4.23	2.0917E−03	6.9619E+00	7.8587E−02	0.0	0.0	0.0	19.84
2.11	1.1394E−04	2.8352E−01	3.2149E−03	4.2	4.6	4.6	155.83
1.06	3.6690E−06	1.0094E−02	1.1388E−04	5.0	4.8	4.8	1236.66
0.53	1.1807E−07	3.3622E−04	3.7828E−06	5.0	4.9	4.9	9957.83
ADER-FV $\mathcal{O}6$, ($M=5$), 2D linear reconstruction							
8.46	1.4291E−02	3.3323E+01	3.9999E−01	0.0	0.0	0.0	5.23
4.23	4.5004E−04	6.7116E−01	8.8316E−03	5.0	5.6	5.5	41.17
2.11	7.6126E−06	1.2672E−02	1.5876E−04	5.9	5.7	5.8	325.58
1.06	1.4174E−07	2.2625E−04	2.7237E−06	5.7	5.8	5.9	2585.91
ADER-FV $\mathcal{O}7$, ($M=6$), 2D linear reconstruction							
8.46	4.8471E−03	1.5521E+01	1.7701E−01	0.0	0.0	0.0	9.48
4.23	8.0981E−05	2.1353E−01	2.4725E−03	5.9	6.2	6.2	73.84
2.11	1.7789E−06	2.8589E−03	3.3622E−05	5.5	6.2	6.2	590.53
1.06	1.6302E−08	2.9101E−05	3.4093E−07	6.8	6.6	6.6	4686.48

choice of the parameters r and ϵ, see [25,23,27,3]. In our new approach, we added a third parameter λ_1, therefore we first perform a sensitivity analysis of the solution with respect to the linear weight on the central stencil λ_1. We compute the advection of a slotted cylinder solving the linearized Euler equations ($\gamma = 1.4$, $\rho_0 = 1$, $p_0 = \frac{1}{\gamma}$) in a two-dimensional computational domain $\Omega = [-50;50]\times[-50;50]$ with four periodic boundary conditions along the diagonal with speeds $u_0 = v_0 = 1$ up to time $t = 25$ using a fourth order WENO reconstruction as described in Section 2.3. The parameter λ_1 is varied between 10^2 and 10^5. The results are presented in Figs. 6 and 7. For comparison, the initial condition as well as the results obtained with a linear reconstruction based only on the central stencil are shown. Our computational mesh is the same as used for the two-dimensional convergence studies, see Fig. 4 (top), with five successive red-refinements [28,21,22]. The initial condition is zero everywhere except for the density perturbation (i.e. the first component of the system of linearized Euler equations) which is a slotted cylinder with center $(-25,-25)$, radius $R = 15$, amplitude 4, slot width 6 and slot length 22, similar to the one proposed by Zalesak [48]. We can see that the solution does not depend much on the choice of λ_1. Despite of the extremely large linear weight on the central stencil in the last case ($\lambda_1 = 10^5$), the solution remains essentially non-oscillatory. This can be explained by the fact that even a very large linear weight of 10^5 is very small compared to the huge nonlinear weights $\tilde{\omega}$ generated for smooth one-sided stencils where the oscillation indicators are almost zero. In smooth regions of the compu-

Table 6
Two-dimensional ADER finite volume schemes from second to seventh order in space and time using the new nonlinear WENO reconstruction based on the central stencil, three primary sector stencils and three reverse sector stencils

h	L^∞	L^1	L^2	$\mathcal{O}_{L^\infty}$	$\mathcal{O}_{L^1}$	$\mathcal{O}_{L^2}$	t_{CPU} [s]
ADER-FV $\mathcal{O}2$, ($M=1$), 2D WENO reconstruction							
4.23	4.6849E−01	2.1506E+03	2.5602E+01	0.0	0.0	0.0	10.92
2.11	1.9165E−01	8.2690E+02	9.3984E+00	1.3	1.4	1.4	84.16
1.06	6.3768E−02	1.8430E+02	2.4600E+00	1.6	2.2	1.9	638.33
0.53	1.0877E−02	1.8786E+01	2.9573E−01	2.6	3.3	3.1	5129.17
ADER-FV $\mathcal{O}3$, ($M=2$), 2D WENO reconstruction							
4.23	4.7998E−02	2.1560E+02	2.3864E+00	0.0	0.0	0.0	14.61
2.11	7.5157E−03	2.9427E+01	3.2864E−01	2.7	2.9	2.9	112.95
1.06	9.2423E−04	3.7963E+00	4.2512E−02	3.0	3.0	3.0	896.02
0.53	1.1617E−04	4.8333E−01	5.4103E−03	3.0	3.0	3.0	7158.27
ADER-FV $\mathcal{O}4$, ($M=3$), 2D WENO reconstruction							
4.23	6.2878E−03	1.0512E+01	1.3217E−01	0.0	0.0	0.0	21.25
2.11	4.8132E−04	5.9663E−01	7.6874E−03	3.7	4.1	4.1	166.80
1.06	3.7761E−05	3.3488E−02	4.3342E−04	3.7	4.2	4.1	1327.34
0.53	2.4868E−06	2.0627E−03	2.6270E−05	3.9	4.0	4.0	10535.64
ADER-FV $\mathcal{O}5$, ($M=4$), 2D WENO reconstruction							
8.46	3.5396E−02	1.3243E+02	1.4796E+00	0.0	0.0	0.0	4.81
4.23	2.2376E−03	7.5768E+00	8.4448E−02	4.0	4.1	4.1	39.59
2.11	1.2066E−04	3.3915E−01	3.8338E−03	4.2	4.5	4.5	311.52
1.06	4.1017E−06	1.2141E−02	1.3691E−04	4.9	4.8	4.8	2477.45
ADER-FV $\mathcal{O}6$, ($M=5$), 2D WENO reconstruction							
8.46	1.3100E−02	3.2971E+01	3.9011E−01	0.0	0.0	0.0	8.17
4.23	5.1919E−04	9.8502E−01	1.2550E−02	4.7	5.1	5.0	70.25
2.11	9.2713E−06	2.0193E−02	2.4820E−04	5.8	5.6	5.7	558.78
1.06	2.4935E−07	3.5281E−04	4.2227E−06	5.2	5.8	5.9	4424.42
ADER-FV $\mathcal{O}7$, ($M=6$), 2D WENO reconstruction							
8.46	4.7807E−03	1.5624E+01	1.7762E−01	0.0	0.0	0.0	12.81
4.23	1.1429E−04	2.2782E−01	2.6894E−03	5.4	6.1	6.0	120.75
2.11	2.8930E−06	1.6990E−03	2.2838E−05	5.3	7.1	6.9	983.64
1.06	4.2599E−08	1.1918E−05	1.6911E−07	6.1	7.2	7.1	7863.11

tational domain, where the oscillation indicators of all stencils take similar values, the central stencil is weighted so heavily that our WENO scheme automatically switches to central reconstruction.

In order to support this conjecture, we next perform a parameter study of the influence of the linear weight λ_1 on the central stencil for a smooth problem. We suppose that the error norms do not depend much on the choice of λ_1, provided it is chosen large enough so that in smooth regions the central stencil will always be the preferred one. The calculated test-problem is the same as used for the two-dimensional convergence studies presented in Section 4. We calculate the problem on the irregular triangular mesh (see Fig. 4 top) with $h = 2.11$ using a fourth order WENO reconstruction and varying λ_1 from 10^2 to 10^5. The results of the error norms are given in Table 9 and show that the error norms are not very sensitive to the choice of this parameter in the studied range. A larger value of λ_1 leads to results that are closer to the ones of a linear reconstruction based only on the central stencil, see Table 5. We note that for all the other calculations done in this article, we set $\lambda_1 = 10^3$.

5.2. Two-dimensional test case

To validate our numerical scheme, we solve the kinematic frontogenesis problem arising in meteorology, as described in [24,9,45], in two space dimensions. It is of particular interest since it allows to check whether a

Table 7
Three-dimensional ADER finite volume schemes from second to sixth order in space and time using a linear reconstruction based only on the central stencil

h	L^∞	L^1	L^2	$\mathcal{O}_{L^\infty}$	$\mathcal{O}_{L^1}$	$\mathcal{O}_{L^2}$	t_{CPU} [s]
ADER-FV $\mathcal{O}2$, ($M=1$), 3D linear reconstruction							
8.67	3.9310E−01	2.0287E+05	2.2694E+02	0.0	0.0	0.0	12.56
4.33	9.7328E−02	5.2193E+04	5.8266E+01	2.0	2.0	2.0	193.84
3.47	6.1320E−02	3.3556E+04	3.7281E+01	2.1	2.0	2.0	474.50
2.17	2.3352E−02	1.3070E+04	1.4545E+01	2.1	2.0	2.0	3029.77
ADER-FV $\mathcal{O}3$, ($M=2$), 3D linear reconstruction							
8.67	2.8633E−01	1.6749E+05	1.8619E+02	0.0	0.0	0.0	24.25
4.33	4.2756E−02	2.3741E+04	2.6338E+01	2.7	2.8	2.8	380.05
3.47	2.1244E−02	1.2234E+04	1.3567E+01	3.1	3.0	3.0	922.58
2.89	1.2676E−02	7.0887E+03	7.8645E+00	2.8	3.0	3.0	1861.53
ADER-FV $\mathcal{O}4$, ($M=3$), 3D linear reconstruction							
8.67	6.8594E−02	3.8995E+04	4.2856E+01	0.0	0.0	0.0	60.16
5.78	1.3391E−02	7.6728E+03	8.6408E+00	4.0	4.0	3.9	302.27
4.33	4.3484E−03	2.4809E+03	2.7468E+00	3.9	3.9	4.0	951.73
3.47	1.8250E−03	1.0099E+03	1.1272E+00	3.9	4.0	4.0	2291.09
ADER-FV $\mathcal{O}5$, ($M=4$), 3D linear reconstruction							
8.67	5.4065E−02	3.0689E+04	3.4014E+01	0.0	0.0	0.0	174.86
5.78	7.8493E−03	4.2487E+03	4.7029E+00	4.8	4.9	4.9	861.44
4.33	1.7343E−03	1.0173E+03	1.1257E+00	5.2	5.0	5.0	2723.48
3.47	5.9937E−04	3.3390E+02	3.6960E−01	4.8	5.0	5.0	6572.97
ADER-FV $\mathcal{O}6$, ($M=5$), 3D linear reconstruction							
17.33	3.3401E−01	1.7333E+05	1.9119E+02	0.0	0.0	0.0	29.44
8.67	5.2120E−03	2.1788E+03	2.4977E+00	6.0	6.3	6.3	468.97
5.78	4.5961E−04	1.6021E+02	1.8230E−01	6.0	6.4	6.5	2368.50
4.33	8.0776E−05	2.6009E+01	2.9740E−02	6.0	6.3	6.3	7449.00

scheme is able to treat discontinuities that move with respect to each other. We solve the locally linearized Euler equations, where the background values appearing in the Jacobian matrices (51) depend on space. In particular, we set $\rho_0 = p_0 = 1$, and the background velocity field in the x–y plane is given as follows:

$$u_0 = -y\omega(r), \quad v_0 = x\omega(r), \quad \omega(r) = \frac{1}{r}U_T(r), \quad r = \sqrt{x^2+y^2},$$
$$U_T(r) = U_{\max}\,\mathrm{sech}^2(r)\tanh(r), \quad U_{\max} = 2.5980762. \tag{54}$$

The discontinuous initial condition depends only on y and reads as

$$u_p(x,y,z,0) = (\,q_0(y) \quad 0 \quad 0 \quad 0 \quad 0\,)^{\mathrm{T}}, \tag{55}$$

with

$$q_0(y) = \begin{cases} -1 & \text{if } y < 0, \\ 1 & \text{if } y \geqslant 0, \end{cases} \tag{56}$$

The exact solution is then given according to [9,45] as follows:

$$u_p(x,y,z,t) = (\,q_0(y\cos(\omega(r)t) - x\sin(\omega(r)t)) \quad 0 \quad 0 \quad 0 \quad 0\,)^{\mathrm{T}}. \tag{57}$$

We note that with growing time t the solution will develop smaller and smaller scales that may become too small to be resolved on a fixed computational mesh. We solve the problem on a computational domain Ω being a circle with radius $R = 5$ and compute the solution up to $t = 6$ using three different triangulations with characteristic mesh lengths $h = 0.04$, $h = 0.02$ and $h = 0.01$ respectively. The coarsest triangulation is depicted in Fig. 8. A 3D plot of the numerical solution obtained on the finest mesh using a sixth order ADER-FV

Table 8
Three-dimensional ADER finite volume schemes from second to sixth order in space and time using the new nonlinear WENO reconstruction based on the central stencil, four primary sector stencils and four reverse sector stencils

h	L^∞	L^1	L^2	$\mathcal{O}_{L^\infty}$	$\mathcal{O}_{L^1}$	$\mathcal{O}_{L^2}$	t_{CPU} [s]
ADER-FV $\mathcal{O}2$, ($M=1$), 3D WENO reconstruction							
8.67	8.8754E−01	5.5942E+05	6.1425E+02	0.0	0.0	0.0	22.63
4.33	4.4800E−01	2.2221E+05	2.7028E+02	1.0	1.3	1.2	354.77
3.47	3.1743E−01	1.4416E+05	1.7769E+02	1.5	1.9	1.9	865.80
2.17	1.5390E−01	8.3702E+04	9.4204E+01	1.5	1.2	1.4	5771.13
ADER-FV $\mathcal{O}3$, ($M=2$), 3D WENO reconstruction							
8.67	5.8007E−01	1.9999E+05	2.3457E+02	0.0	0.0	0.0	45.95
4.33	4.1463E−02	2.3134E+04	2.5158E+01	3.8	3.1	3.2	729.14
3.47	2.0741E−02	1.2019E+04	1.3129E+01	3.1	2.9	2.9	1778.48
2.89	1.1997E−02	6.9421E+03	7.6211E+00	3.0	3.0	3.0	3676.81
ADER-FV $\mathcal{O}4$, ($M=3$), 3D WENO reconstruction							
8.67	1.5419E−01	5.9099E+04	6.7128E+01	0.0	0.0	0.0	119.58
5.78	2.5149E−02	7.4936E+03	9.3283E+00	4.5	5.1	4.9	604.97
4.33	4.7691E−03	2.4376E+03	2.7306E+00	5.8	3.9	4.3	1904.85
3.47	1.9369E−03	9.9601E+02	1.1067E+00	4.0	4.0	4.0	4585.50
ADER-FV $\mathcal{O}5$, ($M=4$), 3D WENO reconstruction							
8.67	7.2843E−02	4.1809E+04	4.6713E+01	0.0	0.0	0.0	286.14
5.78	8.4212E−03	4.2050E+03	4.7182E+00	5.3	5.7	5.7	1426.48
4.33	1.8673E−03	1.0474E+03	1.1463E+00	5.2	4.8	4.9	4510.00
3.47	6.1997E−04	3.5708E+02	3.9116E−01	4.9	4.8	4.8	10885.00
ADER-FV $\mathcal{O}6$, ($M=5$), 3D WENO reconstruction							
17.33	3.3401E−01	1.7333E+05	1.9119E+02	0.0	0.0	0.0	33.00
8.67	8.3475E−03	1.8396E+03	2.2675E+00	5.3	6.6	6.4	525.72
5.78	5.0654E−04	1.7860E+02	2.1058E−01	6.9	5.8	5.9	2655.13
4.33	1.4281E−04	5.5164E+01	6.4060E−02	4.4	4.1	4.1	8350.47

scheme is shown in Fig. 9 for different output times. One can see the rolling of the initial discontinuity and the development of finer and finer scales. The results are very sharp and clearly show the essentially non-oscillatory behavior of the method. To assess this property in more detail, we show one-dimensional cuts through the solution at time $t = 6.0$ along the y-axis ($x = 0$) in Fig. 10 for ADER-FV schemes from second to sixth order of accuracy in space and time. The cuts are taken evaluating the reconstructed solution w_h point-wise on a fixed set of 200 equidistant sampling points in the interval $y \in [-3;3]$. One can make two main observations: First, the higher order schemes in general show a sharper resolution even of the discontinuities than the lower order schemes. Second, as expected for WENO methods, very high order schemes tend to produce oscillations on coarse grids since they need larger stencils which may not fit any more in between the discontinuities. We note that in our approach we do *not* switch to lower order stencils if no smooth high order stencils can be found but we rather rely on mesh refinement. Those oscillations can be clearly seen for example in Fig. 10 (top) for the third order ($M = 2$) and the sixth order ($M = 5$) method. However, after grid refinement the oscillations disappear completely, see Fig. 10 (middle) and (bottom). The numerical results show furthermore that the second-order scheme produces similar results on the finest grid ($h = 0.01$) compared with the sixth order scheme on the intermediate grid ($h = 0.02$).

5.3. Three-dimensional test cases

To our knowledge, there has been no three-dimensional unstructured WENO scheme reported in the research literature up to now. In this section we present the results obtained with a fourth order ADER-FV scheme on unstructured three-dimensional tetrahedral meshes using the previously presented WENO reconstruction.

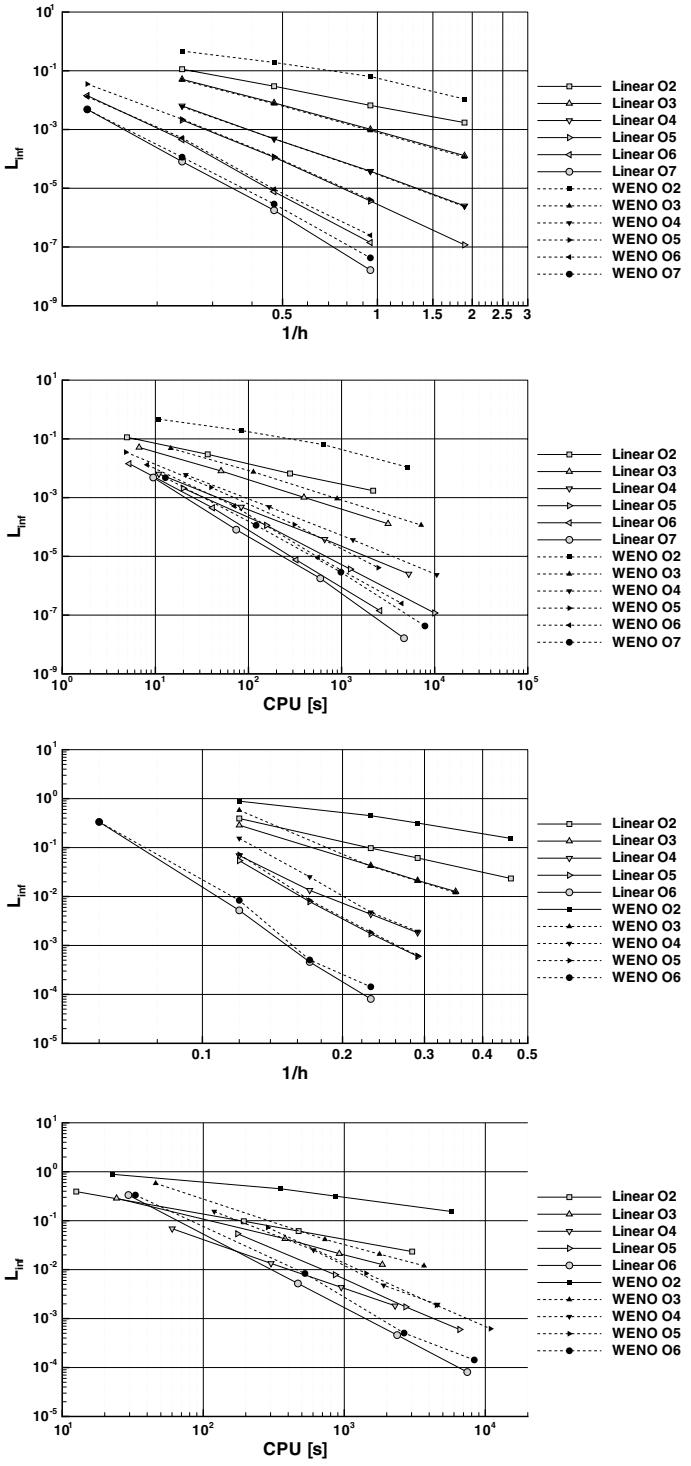

Fig. 5. Numerical convergence behavior of two-dimensional (top) and three-dimensional (bottom) ADER-FV schemes with linear and nonlinear WENO reconstruction in terms of reciprocal mesh spacing $1/h$ and CPU time.

5.3.1. 3D advection example

The first test case consists in the advection of a hollow sphere in a three-dimensional computational domain $\Omega_{3D} = [-50;50] \times [-50;50] \times [-50;50]$ with six periodic boundary conditions. We solve the linearized Euler

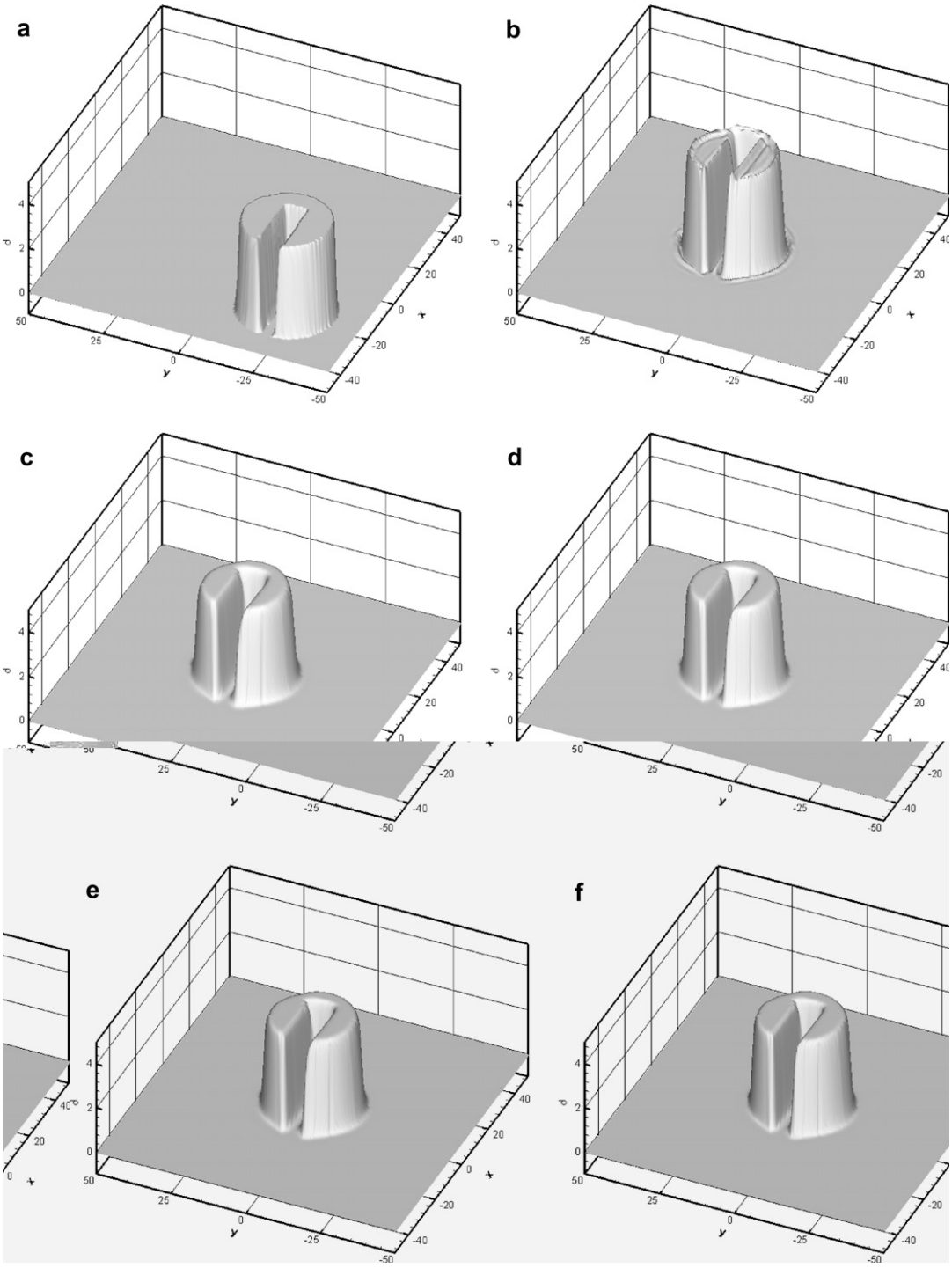

Fig. 6. Sensitivity study of the new WENO parameter λ_1 using fourth order schemes: (a) Initial condition, (b) ADER-FV $\mathcal{O}4$ using linear reconstruction, (c) ADER-FV $\mathcal{O}4$ using WENO with $\lambda_1 = 10^2$, (d) ADER-FV $\mathcal{O}4$ using WENO with $\lambda_1 = 10^3$, (e) ADER-FV $\mathcal{O}4$ using WENO with $\lambda_1 = 10^4$, (f) ADER-FV $\mathcal{O}4$ using WENO with $\lambda_1 = 10^5$.

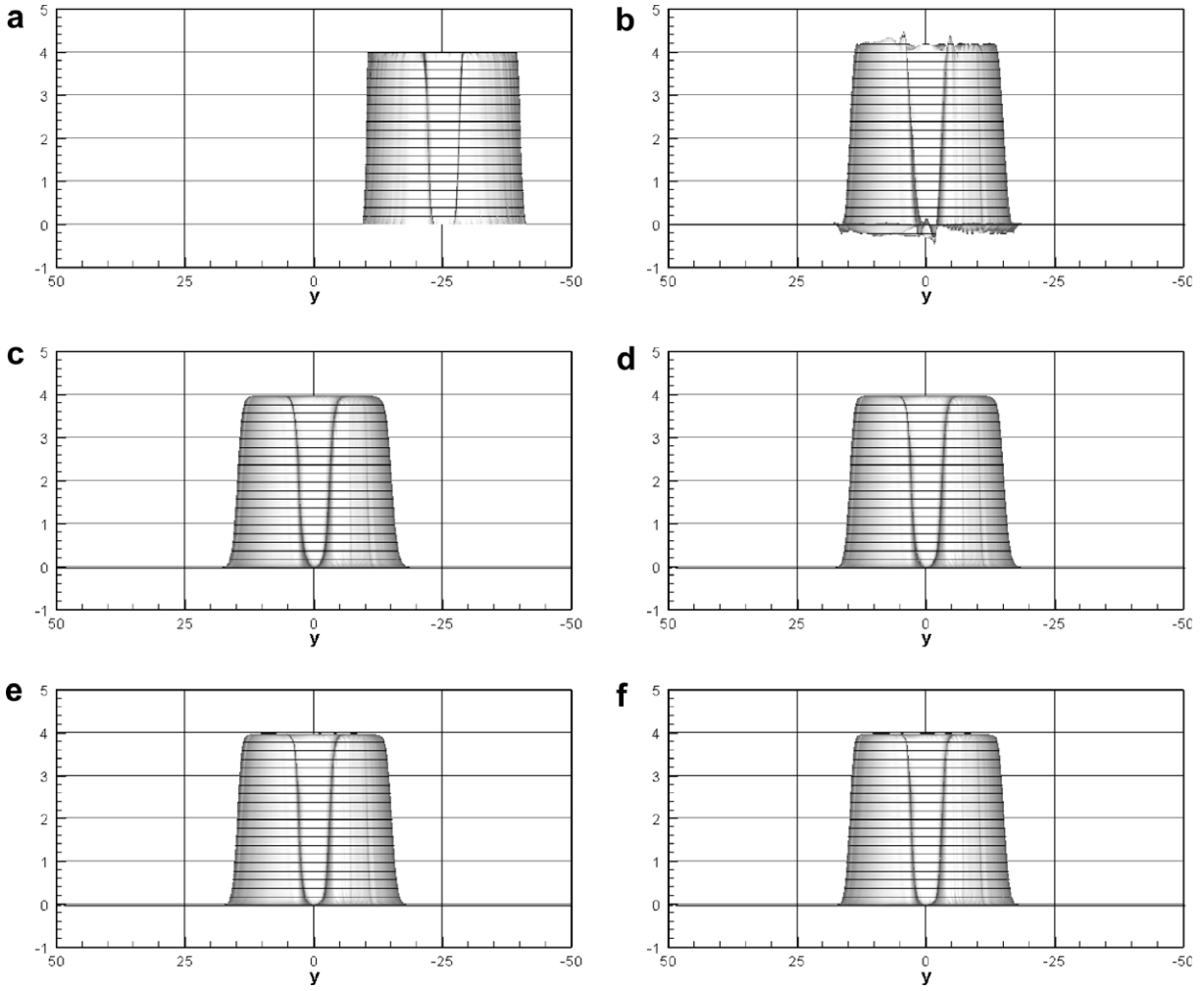

Fig. 7. Sensitivity study of the new WENO parameter λ_1 using fourth order schemes: (a) Initial condition, (b) ADER-FV $\mathcal{O}4$ using linear reconstruction, (c) ADER-FV $\mathcal{O}4$ using WENO with $\lambda_1 = 10^2$, (d) ADER-FV $\mathcal{O}4$ using WENO with $\lambda_1 = 10^3$, (e) ADER-FV $\mathcal{O}4$ using WENO with $\lambda_1 = 10^4$, (f) ADER-FV $\mathcal{O}4$ using WENO with $\lambda_1 = 10^5$.

Table 9
Sensitivity study with respect to the linear weight λ_1 on the central stencil using a two-dimensional fourth order ADER finite volume scheme with WENO reconstruction. Grid spacing is $h = 2.11$

λ_1	L^∞	L^1	L^2
10^2	5.0012E−04	4.9330E−01	6.6470E−03
10^3	4.8132E−04	5.9663E−01	7.6874E−03
10^4	4.7947E−04	6.1402E−01	7.8842E−03
10^5	4.7928E−04	6.1582E−01	7.9047E−03

equations with the same parameters as in the previous convergence and sensitivity studies, i.e. $\gamma = 1.4$, $\rho_0 = 1$, $p_0 = \frac{1}{\gamma}$ and $u_0 = v_0 = w_0 = 1$. The discontinuous initial condition is given as a function of $r = \sqrt{x^2 + y^2 + z^2}$:

$$u_p(x, y, z, 0) = (\, u_1(r) \quad 0 \quad 0 \quad 0 \quad 0 \,)^{\mathrm{T}}, \tag{58}$$

with

$$u_1(r) = \begin{cases} 1 & \text{if } R_i \leqslant r \leqslant R_a, \\ 0 & \text{else}, \end{cases} \tag{59}$$

choosing for the inner radius $R_i = 17$ and for the outer radius $R_a = 34$. After $t = 100$ the exact solution is again given by the initial condition. The problem is solved on an irregular unstructured mesh containing 191933 tetrahedrons, see Fig. 11, where the projection of the discontinuous initial condition is highlighted in dark gray. To visualize the interior of the domain Ω as well as some part of the tetrahedrization, the sector where $x > 0$ and $y > 0$ and $z > 0$ is not plotted. We perform two computations of this test case, always using fourth order ADER-FV schemes and the same numerical parameters, but once using only linear reconstruction based on the central stencil and once the WENO reconstruction proposed in Section 2.3.

The results are plotted in Fig. 12, where we show a cut of the reconstructed initial condition as well as the reconstructed solution after one advection period at $t = 100$ in the x–y plane. To facilitate visualization of the inner discontinuity, the sector where $x > 0$ and $y > 0$ is not plotted. We clearly see the generation of heavy oscillations with the linear reconstruction operator, especially in the reconstruction of the discontinuous initial condition, whereas the WENO scheme is able to obtain a very good non-oscillatory solution. The total CPU time for the calculation using the ADER-FV scheme with WENO reconstruction was only 50% larger than the time needed by the ADER-FV scheme based on the linear reconstruction operator using only the central stencil.

5.3.2. Robustness on highly stretched grids

The second three-dimensional test case is chosen in order to study the robustness of our method with respect to highly stretched grids. There is a very well-known one-dimensional advection test case that is often documented in the research literature on WENO schemes, see [3,25,43] to study the long-time evolution of the numerical solution of the one-dimensional scalar advection equation. In this section, we basically compute the same problem, but solve the linearized Euler equations on two highly distorted three-dimensional tetrahedral grids. The background values in the Jacobian matrices are $\rho_0 = 1$, $u_0 = 1$, $v_0 = w_0 = 0$ and $p_0 = 1$. The computational domain is $\Omega_{3D}(L) = [-1;1] \times [-L;L] \times [-L;L]$ and is in both cases meshed using a regular tetrahedral mesh, see Fig. 4 (bottom) with 400 elements in x-direction and six elements in each y and z-direction. The scaling parameter is $L = 0.3$ for the highly stretched mesh in y and z direction and $L = 0.00075$ for the highly stretched mesh in x direction. The stretching ratio with respect to the corresponding axis direction is in both

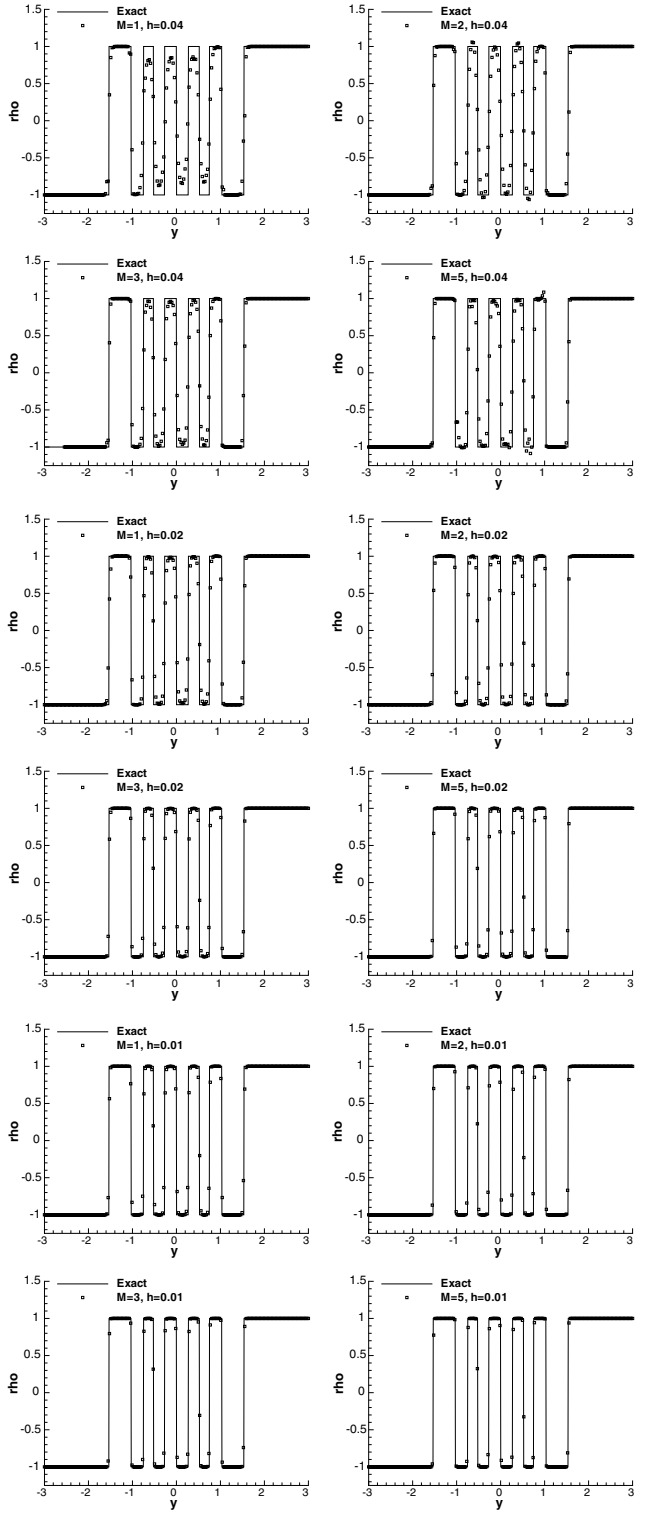

Fig. 10. Kinematic frontogenesis problem: Cut along the y-axis at time $t = 6$. ADER-FV schemes $\mathcal{O}2$ ($M = 1$) up to $\mathcal{O}6$ ($M = 5$). Characteristic mesh lengths $h = 0.04$ (top), $h = 0.02$ (middle), $h = 0.01$ (bottom).

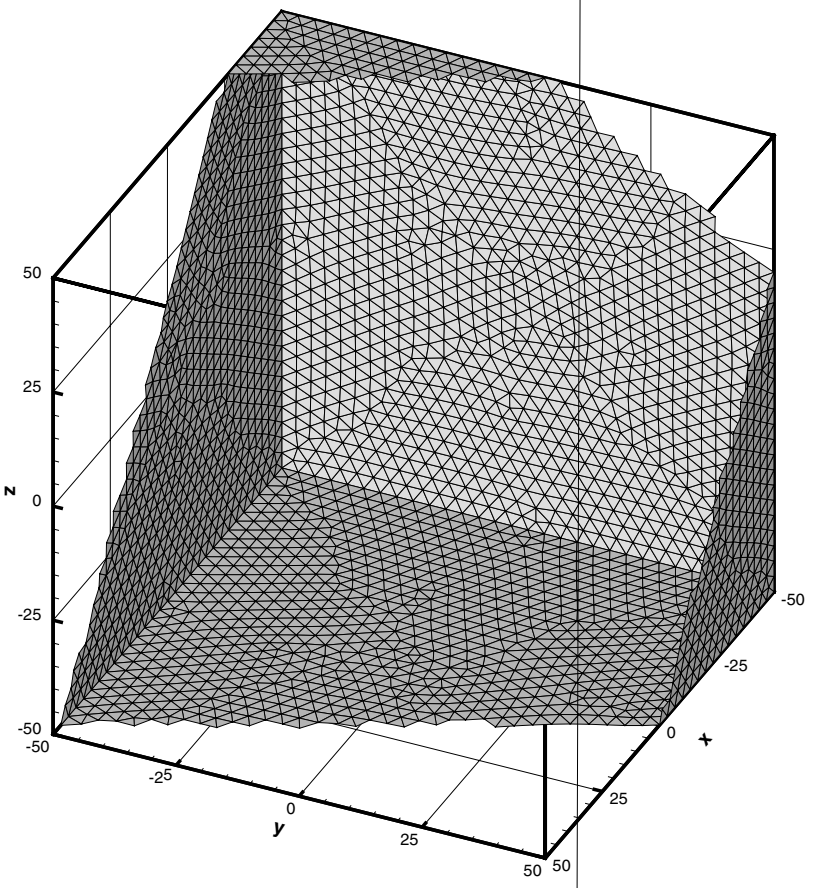

cases 1:20. A representative tetrahedron in physical coordinates of both stretched grids can be seen in Fig. 13 (left) for $L = 0.3$ and in Fig. 13 (right) for $L = 0.00075$. The tetrahedrons on the left of Fig. 13 are very thin plates whereas the tetrahedrons on the right of Fig. 13 are long needles. The advection in this test case is always parallel to the x-axis and therefore with the thin plates and the needles we can check the robustness of the method for advection occurring parallel and normal to the stretched direction, respectively.

The initial condition for the system is zero except of the first component (density fluctuation ρ) which is given according to Jiang and Shu [25] as

$$\rho(x,0) = \begin{cases} \frac{1}{6}[G(x,z-\delta) + G(x,z+\delta) + 4G(x,z)], & -0.8 \leqslant x \leqslant -0.6; \\ 1, & -0.4 \leqslant x \leqslant -0.2; \\ 1 - |10(x-0.1)|, & 0.0 \leqslant x \leqslant 0.2; \\ \frac{1}{6}[F(x,a-\delta) + F(x,a+\delta) + 4F(x,a)], & 0.4 \leqslant x \leqslant 0.6; \\ 0, & \text{otherwise}, \end{cases}$$

with $G(x,z) = \mathrm{e}^{-\beta(x-z)^2}$ and $F(x,a) = \sqrt{\max(1-\alpha^2(x-a)^2, 0)}$.

The constants are $a = 0.5$, $z = -0.7$, $\delta = 0.005$, $\alpha = 10$ and $\beta = \frac{\ln 2}{36\delta^2}$, see [25]. We impose six periodic boundary conditions and compute the numerical solution up to time $t = 20$, which corresponds to ten periods of advection. The results are depicted in Fig. 14 as 1D cuts through the reconstructed solution w_h on 800 equidistant sample points along the x-axis ($x \in [-1;1]$) for ADER-FV schemes from second to fourth order of accuracy. We can clearly observe the improvement of the resolution of smooth features with increasing order of accuracy as well as the essentially non-oscillatory behavior of the scheme, even on these highly stretched

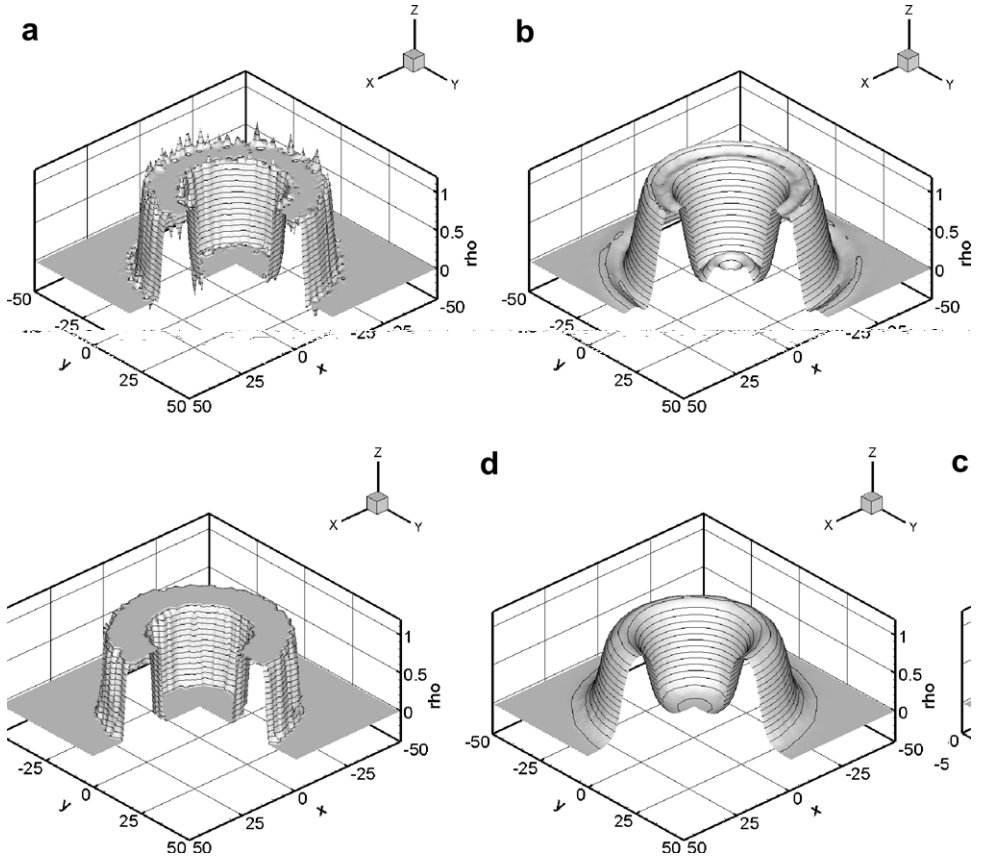

Fig. 12. Results in the cutting plane $z = 0$ of the 3D test case using fourth order ADER-FV schemes: (a) Reconstructed initial condition using linear reconstruction. (b) Reconstructed solution at $t = 100$ using linear reconstruction. (c) Reconstructed initial condition using WENO reconstruction. (d) Reconstructed solution at $t = 100$ using WENO reconstruction.

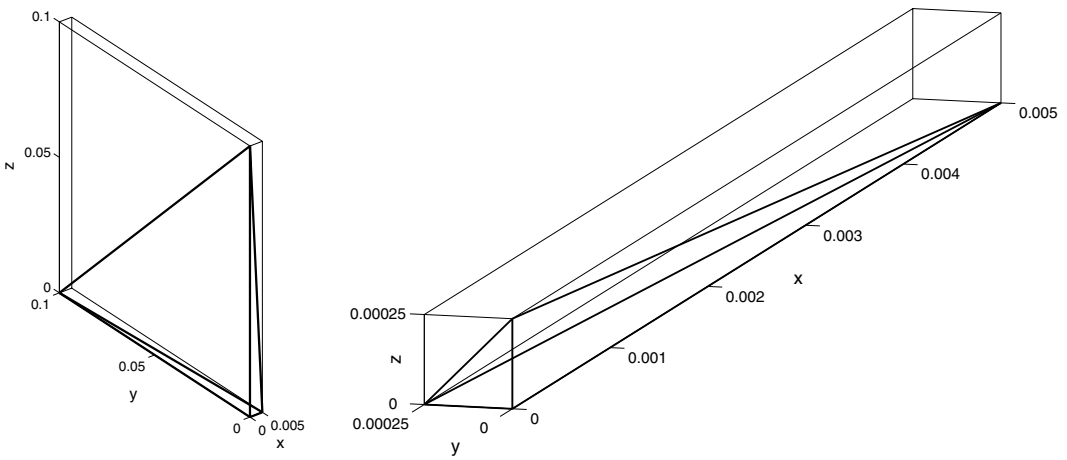

Fig. 13. Stretched tetrahedrons in physical coordinates for the thin plates with $L = 0.3$ (left) and the needles with $L = 0.00075$ (right). The aspect ratio of the shortest and the longest edge is in both cases 1:20.

grids. We emphasize that even in such stretched grids the reconstruction stencils will be mapped to regular stencils in the reference coordinate system, in which the final reconstruction equations are written and solved. Please note that such badly stretched tetrahedrons (usually called slivers) can actually appear in unstructured

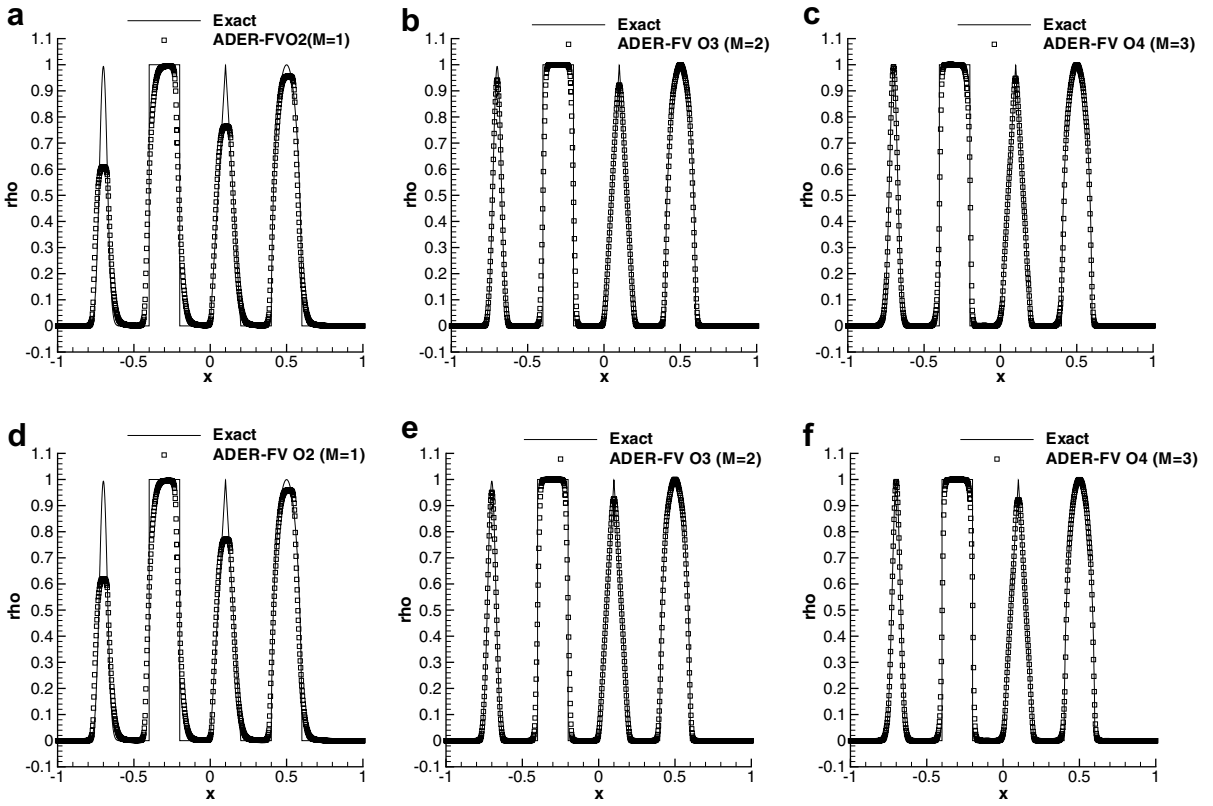

Fig. 14. Cuts trough the reconstructed solution w_h along the x-axis on 800 equidistant sample points after ten periods ($t = 20$) for the advection test on stretched grids. (a)–(c): Thin plates ($L = 0.3$); (d)–(f): Needles ($L = 0.00075$).

3D mesh generation, e.g. near corners of solid wall boundaries or at the intersection of differently meshed subzones of the grid.

6. Summary and conclusions

In this article we presented a new reconstruction procedure of arbitrary accuracy for finite volume schemes on unstructured meshes in two and three space dimensions. For the reconstruction we use hierarchical orthogonal basis functions of degree M, as frequently used in the discontinuous Galerkin finite element framework. This leads to a scheme with an order of accuracy $M + 1$. The output of the reconstruction is an entire polynomial, not a point-value on a specific location, which commonly is the case for several high order reconstructions [25,23,3]. The reconstruction basis is defined in a reference coordinate system and therefore our reconstruction essentially relies on the transformation of the physical reconstruction stencils into this particular reference system. This takes out scaling effects that usually may lead to ill-conditioned reconstruction matrices. It was shown that the computation of the reconstruction matrices can be done very generally using basis functions. They can be easily pre-computed by Gaussian quadrature of the basis functions over the stencil and can then be stored for each element. For robustness purposes, more elements than the minimum needed for reconstruction of a polynomial of degree M are used, see also [4,30,27].

After the linear reconstruction had been developed, the step to a nonlinear weighted essentially non-oscillatory (WENO) reconstruction technique that provides an entire polynomial was done. For this purpose, our proposed WENO scheme on unstructured grids uses a nonlinearly weighted sum of polynomials of degree M in order to obtain finally a nonlinear WENO polynomial of equal degree M. The use of basis functions in a reference element allows an efficient computation of the WENO oscillation indicators which become quadratic

functionals of the reconstructed degrees of freedom. The oscillation indicator matrix Σ_{lm} appearing in these functionals is universal and does neither depend on the problem, nor on the mesh. It depends only on the basis functions, the order of accuracy and the number of space dimensions. The set of reconstruction stencils contains one central stencil and a set of purely one-sided primary and reverse sector stencils, see [27]. The linear weights on the one-sided stencils are chosen to be equal to one, and a much larger linear weight λ_1 (typically 10^3) is put on the central stencil which should be the preferred one in smooth regions. This choice for the linear weights avoids the problems of negative linear weights documented previously in the literature on WENO schemes for unstructured meshes [23,36]. The numerical results are quite insensitive with respect to the choice of this new WENO parameter which has been confirmed by numerical experiments with smooth and discontinuous solutions. The availability of the whole polynomial furthermore considerably reduces computational cost in multiple space dimensions, especially if solution-dependent source terms have to be evaluated or if derivatives of the reconstruction have to be computed. In fact, our numerical studies show that in combination with the ADER approach (which essentially relies on derivative information for flux computation) the use of a nonlinear WENO reconstruction instead of a linear reconstruction based on one single central stencil only increases the computational effort by a factor which is not larger than two, see Tables 5–8. This is quite a remarkable result since usually WENO schemes are considered to be very expensive.

However, we must underline the fact that due to this choice of the linear weights the overall accuracy obtained by our WENO method can *not* be the optimal one any more with respect to a WENO scheme using the same set of stencils and optimal linear weights. This is certainly a disadvantage, however we would like to give three arguments to justify our choice: First, our choice of the linear weights simplifies implementation considerably, especially on three-dimensional unstructured tetrahedral grids. The second and even more important argument is the availability of the entire polynomials in the reference element and therefore also of all space derivatives instead of mere point values. The reconstruction in the reference element allows the efficient mesh-independent computation of the oscillation indicators according to (24) and makes furthermore the use of the ADER approach very efficient. Third, an optimal WENO scheme can only be constructed for point-wise reconstruction in the Gaussian integration points on the surfaces, which means that the whole nonlinear WENO reconstruction procedure has to be repeated in each quadrature point. For the moment, we do not yet consider source terms, which would lead to volume integrals and therefore to a further increase in Gaussian integration points. On a tetrahedron in 3D one would have to use e.g. at least seven quadrature points on each triangular surface for a fifth order method (see [38, p. 315]), which makes a total of 28 quadrature points for all four sides and therefore would require 28 optimal WENO reconstructions. Using a third order TVD Runge–Kutta time-stepping method in a method-of-lines (MOL) approach, as usual for standard WENO schemes documented in the literature, one would need *84* optimal WENO reconstructions per element and time step and achieves at the end, however, only a global order of accuracy of three due to the Runge–Kutta time stepping. By contrast, with our ADER-FV approach one obtains full fifth order of accuracy in space and time with only *one* reconstruction per element and time step where the reconstruction yields the entire polynomial with all its derivatives. In our opinion, this last point is the most important advantage of the chosen reconstruction strategy, even more important than the resulting non-negative weights.

The new WENO reconstruction algorithm has been used to construct arbitrary high order finite volume schemes on unstructured meshes in two and three space dimensions using the ADER approach of Toro et al. [42,40,41,35,34] for flux calculation. In this article we restricted us to the solution of linear hyperbolic systems. Practical applications of the scheme may be acoustic, electro-magnetic or seismic wave propagation in complex geometries. However, the same reconstruction technique can be also applied to construct arbitrary high order accurate finite volume schemes for nonlinear hyperbolic systems, which will be subject to a further publication. Another application of the proposed WENO reconstruction that produces entire polynomials may be the use as limiters for discontinuous Galerkin schemes on unstructured meshes, as already proposed by Qiu and Shu [33,31,32] for structured grids.

Acknowledgments

The research presented in this paper was financed by the Deutsche Forschungsgemeinschaft (DFG) in the framework of the *DFG Forschungsstipendium* (DU 1107/1-1), the *Emmy Noether Programm* (KA 2281/1-1)

and the DFG-CNRS research group FOR 508, *Noise Generation in Turbulent Flows*. We would like to thank the two anonymous referees who helped to improve the clarity and the quality of this article and last but not least we thank the HLRS supercomputing center in Stuttgart (Germany) for support and for providing the computing facilities for the 3D test cases.

References

[1] R. Abgrall, On essentially non-oscillatory schemes on unstructured meshes: analysis and implementation, Journal of Computational Physics 144 (1994) 45–58.
[2] H. Atkins, C.W. Shu, Quadrature-free implementation of the discontinuous Galerkin method for hyperbolic equations, AIAA Journal 36 (1998) 775–782.
[3] D. Balsara, C.W. Shu, Monotonicity preserving weighted essentially non-oscillatory schemes with increasingly high order of accuracy, Journal of Computational Physics 160 (2000) 405–452.
[4] T.J. Barth, P.O. Frederickson, Higher order solution of the Euler equations on unstructured grids using quadratic reconstruction. AIAA paper no. 90-0013, 28th Aerospace Sciences Meeting January 1990.
[5] M. Ben-Artzi, J. Falcovitz, A second-order Godunov-type scheme for compressible fluid dynamics, Journal of Computational Physics 55 (1984) 1–32.
[6] J.C. Butcher, The Numerical Analysis of Ordinary Differential Equations: Runge–Kutta and General Linear Methods, Wiley, 1987.
[7] J. Casper, H.L. Atkins, A finite-volume high-order ENO scheme for two-dimensional hyperbolic systems, Journal of Computational Physics 106 (1993) 62–76.
[8] B. Cockburn, G.E. Karniadakis, C.W. Shu, Discontinuous Galerkin MethodsLecture Notes in Computational Science and Engineering, Springer, 2000.
[9] R. Davies-Jones, Comments on 'a kinematic analysis of frontogenesis associated with a non-divergent vortex', Journal of Atmospheric Sciences 42 (1985) 2073–2075.
[10] M. Dubiner, Spectral methods on triangles and other domains, Journal of Scientific Computing 6 (1991) 345–390.
[11] M. Dumbser, Arbitrary High Order Schemes for the Solution of Hyperbolic Conservation Laws in Complex Domains, Shaker Verlag, Aachen, 2005.
[12] M. Dumbser, M. Käser, An arbitrary high order discontinuous Galerkin method for elastic waves on unstructured meshes II: The three-dimensional isotropic case, Geophysical Journal International, in press.
[13] M. Dumbser, C.D. Munz, ADER discontinuous Galerkin schemes for aeroacoustics, Comptes Rendus Mécanique 333 (2005) 683–687.
[14] M. Dumbser, C.D. Munz, Arbitrary high order discontinuous Galerkin schemes, in: S. Cordier, T. Goudon, M. Gutnic, E. Sonnendrucker (Eds.), Numerical Methods for Hyperbolic and Kinetic Problems, IRMA Series in Mathematics and Theoretical Physics, EMS Publishing House, 2005, pp. 295–333.
[15] M. Dumbser, C.D. Munz, Building blocks for arbitrary high order discontinuous Galerkin schemes, Journal of Scientific Computing 27 (2006) 215–230.
[16] M. Dumbser, T. Schwartzkopff, C.D. Munz, Arbitrary high order finite volume schemes for linear wave propagation, in: Computational Science and High Performance Computing IINotes on Numerical Fluid Mechanics and Multidisciplinary Design (NNFM), Springer, 2006, pp. 129–144.
[17] O. Friedrich, Weighted essentially non-oscillatory schemes for the interpolation of mean values on unstructured grids, Journal of Computational Physics 144 (1998) 194–212.
[18] S.K. Godunov, Finite difference methods for the computation of discontinuous solutions of the equations of fluid dynamics, Mathematics of the USSR-Sbornik 47 (1959) 271–306.
[19] A. Harten, High resolution schemes for hyperbolic conservation laws, Journal of Computational Physics 49 (1983) 357–393.
[20] A. Harten, B. Engquist, S. Osher, S.R. Chakravarthy, Uniformly high order accurate essentially non-oscillatory schemes III, Journal of Computational Physics 71 (1987) 231–303.
[21] D. Hempel, Local mesh adaption in two space dimensions, IMPACT Computational Science & Engineering 5 (1993) 309–317.
[22] D. Hempel, Isotropic refinement and recoarsening in 2 dimensions, Technical Report DLR IB 223-95 A 35, Deutsches Zentrum fnr Luft- und Raumfahrt (DLR), 1995.
[23] C. Hu, C.W. Shu, Weighted essentially non-oscillatory schemes on triangular meshes, Journal of Computational Physics 150 (1999) 97–127.
[24] C.A. Doswell III, A kinematic analysis of frontogenesis associated with a non-divergent vortex, Journal of Atmospheric Sciences 41 (1984) 1242–1248.
[25] G.-S. Jiang, C.W. Shu, Efficient implementation of weighted ENO schemes, Journal of Computational Physics (1996) 202–228.
[26] M. Käser, M. Dumbser, An arbitrary high order discontinuous Galerkin method for elastic waves on unstructured meshes I: The two-dimensional isotropic case with external source terms, Geophysical Journal International 166 (2006) 855–877.
[27] M. Käser, A. Iske, ADER schemes on adaptive triangular meshes for scalar conservation laws, Journal of Computational Physics 205 (2005) 486–508.
[28] A. Meister, J. Struckmeier, Hyperbolic Partial Differential Equations, Vieweg, 2002.
[29] C.D. Munz, On the numerical dissipation of high resolution schemes for hyperbolic conservation laws, Journal of Computational Physics 77 (1988) 18–39.

[30] C. Ollivier-Gooch, M. Van Altena, A high-order-accurate unstructured mesh finite-volume scheme for the advection–diffusion equation, Journal of Computational Physics 181 (2002) 729–752.
[31] J. Qiu, C.W. Shu, Hermite WENO schemes and their application as limiters for Runge–Kutta discontinuous Galerkin method: one-dimensional case, Journal of Computational Physics 193 (2003) 115–135.
[32] J. Qiu, C.W. Shu, Hermite WENO schemes and their application as limiters for Runge–Kutta discontinuous Galerkin method II: Two dimensional case, Computers and Fluids 34 (2005) 642–663.
[33] J. Qiu, C.W. Shu, Runge–Kutta discontinuous Galerkin method using WENO limiters, SIAM Journal on Scientific Computing 26 (2005) 907–929.
[34] T. Schwartzkopff, M. Dumbser, C.D. Munz, Fast high order ADER schemes for linear hyperbolic equations, Journal of Computational Physics 197 (2004) 532–539.
[35] T. Schwartzkopff, C.D. Munz, E.F. Toro, ADER: a high order approach for linear hyperbolic systems in 2d, Journal of Scientific Computing 17 (1–4) (2002) 231–240.
[36] J. Shi, C. Hu, C.W. Shu, A technique of treating negative weights in WENO schemes, Journal of Computational Physics 175 (2002) 108–127.
[37] T. Sonar, On the construction of essentially non-oscillatory finite volume approximations to hyperbolic conservation laws on general triangulations: polynomial recovery, accuracy and stencil selection, Computer Methods in Applied Mechanics and Engineering 140 (1997) 157–181.
[38] A.H. Stroud, Approximate Calculation of Multiple Integrals, Prentice-Hall Inc., Englewood Cliffs, NJ, 1971.
[39] P.K. Sweby, High resolution TVD schemes using flux limiters, Lecture Notes in Applied Mathematics 22 (1985) 289–309.
[40] V.A. Titarev, E.F. Toro, ADER: arbitrary high order Godunov approach, Journal of Scientific Computing 17 (1–4) (2002) 609–618.
[41] V.A. Titarev, E.F. Toro, ADER schemes for three-dimensional nonlinear hyperbolic systems, Journal of Computational Physics 204 (2005) 715–736.
[42] E.F. Toro, R.C. Millington, L.A.M. Nejad, Towards very high order Godunov schemes, in: E.F. Toro (Ed.), Godunov Methods. Theory and Applications, Kluwer/Plenum Academic Publishers, 2001, pp. 905–938.
[43] E.F. Toro, V. Titarev, TVD fluxes of the high-order ADER schemes, Journal of Scientific Computing 24 (2005) 285–309.
[44] E.F. Toro, V.A. Titarev, Solution of the generalized Riemann problem for advection-reaction equations, Proceedings of Royal Society of London (2002) 271–281.
[45] E.F. Toro, V.A. Titarev, ADER schemes for scalar hyperbolic conservation laws with source terms in three space dimensions, Journal of Computational Physics 202 (2005) 196–215.
[46] B. van Leer, Towards the ultimate conservative difference scheme II: Monotonicity and conservation combined in a second order scheme, Journal of Computational Physics 14 (1974) 361–370.
[47] B. van Leer, Towards the ultimate conservative difference scheme V: a second order sequel to Godunov's method, Journal of Computational Physics 32 (1979) 101–136.
[48] S.T. Zalesak, Fully multidimensional flux-corrected transport algorithms for fluids, Journal of Computational Physics 31 (1979) 335–362.